confirmed the binding of RUNX-2 to the HY box (Figure 5A).

Mutagenesis analyses in the HY box oligonucleotide probe showed that complex formation was abolished by the mutations inside the identified responsive region (from −81 bp to −76 bp) (mutations 2 and 3 in Figure 4), but not by mutations outside the region (Figure 5B). Cold competition with an excess amount of the unlabeled wild-type and outside mutation probes suppressed complex formation, while competition with the unlabeled inside mutation probes did not affect it (Figure 5B). These results demonstrate the specific binding between RUNX-2 and the identified responsive region (from −81 bp to −76 bp) of the HY box.

ChIP assay showed in vivo binding of RUNX-2 to the COL10A1 promoter regulatory region, including the HY box, in the presence of CBFβ (Figure 5C). Specificity was confirmed as RUNX-2 because it was not immunoprecipitated in the absence of the antibody or by the negative control nonimmune IgG.

Involvement of other RUNX-2 binding motifs in the activation of the human COL10A1 promoter by RUNX-2. Next, we screened for other possible RUNX-2 binding motifs with the putative consensus sequences (20) in the 4.5-kb fragment of the 5′-end flanking region of the human COL10A1 promoter. Of the 6 identified regions, we selected the 2 most probable regions. The region from −1,839 bp to −1,834 bp was shown by comparative genomic analysis to correspond to the core responsive element of RUNX-2 in the mouse Col10a1 promoter identified in a previous study (20), and the region from −357 to −352 was the most proximal to the transcription start site of the 6 regions. We then prepared the 30-bp elements that included these 2 regions for further analyses, and called them A box (from −1,849 bp to −1,820 bp) and B box (from −369 bp to −340 bp) (Figure 6).

When we compared the dose-response effects of the tandem repeats on luciferase activity using the 3 human cell lines as described above, neither the A box nor the B box responded to RUNX-2 alone or to RUNX-2 in combination with CBFβ regardless of the number of repeats, in contrast to the HY box, which showed potent repeat number–dependent increases (Figure 6A). In addition to the 3 human elements, we examined binding of the partially or fully mutated HY box probe to the corresponding mouse sequence with RUNX-2 by EMSA. None of the mutated HY box probes formed a complex with the nuclear extract of RUNX-2 and CBFβ-transfected cells (Figure 6B), similar to mutation 2 in Figure 5B. However, both A box and B box oligonucleotide probes did form complexes with the nuclear extracts, which were supershifted by addition of an antibody to RUNX-2, indicating the specific binding of RUNX-2 to all human wild-type elements: HY box, A box, and B box (Figure 6B). More interestingly, when in vivo binding of RUNX-2 to the 3 elements was examined by ChIP assay using human HuH7 cells, RUNX-2 bound to the COL10A1 promoter region that included the HY box, but not to the region including the A box or B box or to the region without the putative RUNX-2 binding motif (Figure 6C).

The results of luciferase assay, EMSA, and ChIP suggested that the HY box was the principal responsive element of RUNX-2 under specific epigenetic environments in human cells. In fact, when we used mouse chondrogenic ATDC-5 cells instead of human cells for the luciferase assays, neither RUNX-2 alone nor a combination of RUNX-2 and CBFβ affected COL10A1 promoter activity. (Data are available online at http://www.h.u-tokyo.ac.jp/ortho/Supplemental_Figures.pdf.) Interestingly, however, there was a decrease in the region between −81 bp and −76 bp in not only RUNX-2–induced activity, but also basal promoter activity. Furthermore, luciferase assays of the tandem repeats of the human elements showed a moderate but repeat number–dependent increase in HY box activity in ATDC-5 cells whether or not they were transfected with RUNX-2, although neither the mutated HY box (mutation 2), A box, nor B box showed the response. (Data are available online at http://www.h.u-tokyo.ac.jp/ortho/Supplemental_Figures.pdf.) Hence, the HY box may also function as a basal responsive element for various transcriptional stimulations regardless of species.

DISCUSSION

The present study showed that human COL10A1 promoter activity was enhanced by RUNX-2 alone and was enhanced even more potently by RUNX-2 in combination with the coactivator CBFβ, and further identified the HY box as the principal and specific responsive element in the 3 human cell lines. Although this is the first study to identify the promoter element responsive to RUNX-2 in the human COL10A1 gene, RUNX-2 binding sites have previously been identified at more distal regions in the mouse Col10a1 promoter (20), which is not within the highly conserved region between mouse and human genes (Figure 3A). The human promoter region that corresponds to the mouse responsive element (A box) showed little response to RUNX-2 and did not show in vivo binding with RUNX-2 in

human cells (Figures 6A and C). The mouse promoter region that corresponds to the human HY box did not bind to RUNX-2 (Figure 6B), and the human HY box did not respond to RUNX-2 in mouse ATDC-5 cells. (Data are available online at http://www.h.u-tokyo.ac.jp/ortho/Supplemental_Figures.pdf.) These findings indicate that there are different mechanisms of type X collagen transactivation by RUNX-2 in humans and mice, and demonstrate that RUNX-2 binds to and activates the HY box in the specific microenvironment in human cells.

Nevertheless, the present study showed the colocalization of RUNX-2 and type X collagen in mouse specimens (Figure 1) and the induction of endogenous type X collagen expression by RUNX-2 in mouse cells (Figure 2). Our study had inevitable limitations, since neither human samples during endochondral ossification nor human chondrogenic cell lines that undergo hypertrophic differentiation are available. Indeed, the endogenous type X collagen induction in mouse cells by RUNX-2 shown in Figure 2 may not be due to transactivation of the mouse HY box, but to transactivation of the responsive element identified in a previous mouse study (20). However, mutations in the RUNX-2 gene cause cleidocranial dysplasia in both humans and mice (32,34,35). In addition, mutations in the COL10A1 gene cause skeletal abnormalities similar to Schmid-type metaphyseal chondrodysplasia in both species (9–12). We therefore believe that RUNX-2 and type X collagen play a role in endochondral ossification in humans as well as in mice.

The temporal and spatial specificity of type X collagen expression has been shown to be under the tight control of positive and negative regulators. In contrast to the positive regulator RUNX-2, parathyroid hormone (PTH) and PTH-related protein (PTHrP) are known to be crucial inhibitors of transcription (36–38). Previous searches in the human COL10A1 promoter have located a regulatory region between −2,410 bp and −1,875 bp upstream of the transcription start site, the activity of which was suppressed by PTH/PTHrP (38–42). In the central part of the region, a functional activator protein 1 (AP-1) site was identified between −2,144 bp and −2,135 bp as a responsive region of FosB and Fra-1 (42). Another enhancer region was identified between −2,273 bp and −2,244 bp, although the related transcription factor remains unknown (41). The deletion analysis of the luciferase assay that was performed in the present study, however, failed to detect a decrease in activity between −2,349 bp and −1,899 bp, which contains the 2 above-mentioned regions, with or without RUNX-2 transfection in any cell line (Figure 3B), indicating a different mechanism of RUNX-2 transcriptional regulation than of PTH/PTHrP and AP-1 transcriptional regulation in humans.

For the examination of RUNX-2 localization in the limb cartilage and the bone fracture callus, we used X-Gal staining in heterozygous *Runx2*-deficient mice with *lacZ* gene insertion at the *Runx2*-deletion site ($Runx2^{+/lacZ}$ mice) (32). This is because neither antibodies nor riboprobes worked appropriately in the localization of RUNX-2 by immunostaining or in situ hybridization, respectively, of the tissue of wild-type mice. Our preliminary studies confirmed that the $Runx2^{+/lacZ}$ mice showed normal skeletal phenotypes, except that they exhibited a dysplastic clavicle, which is typical of cleidocranial dysplasia, as previously reported (32) (Details are available online at http://www.h.u-tokyo.ac.jp/ortho/Supplemental_Figures.pdf.) Their growth plate phenotypes were also comparable with those of their wild-type littermates before and after birth. In addition, fracture callus formation and type X collagen expression in the callus were similar between the 2 genotypes.

These findings indicate that the RUNX-2 haploinsufficiency in $Runx2^{+/lacZ}$ mice did not cause abnormalities in skeletal growth or repair, confirming the adequacy of using $Runx2^{+/lacZ}$ mice instead of wild-type mice for the analysis. However, in a previous study in which we created an experimental OA model by induction of knee joint instability, $Runx2^{+/lacZ}$ mice exhibited suppression of type X collagen expression and degradation in joint cartilage (22). The fact that RUNX-2 haploinsufficiency prevented OA progression without affecting physiologic skeletal growth and repair suggests that RUNX-2–related signaling can be a therapeutic target of this disorder without severe skeletal side effects.

The HY box is indeed a core promoter element in the human COL10A1 gene responsive to RUNX-2 in human cells. However, basal luciferase activity without RUNX-2 transfection was also decreased in the region between −81 bp and −76 bp in the HY box not only in mouse ATDC-5 cells, but also in 3 human cell lines (Figure 3B), although not to as great an extent as RUNX-2–induced activity. Furthermore, the site-directed mutagenesis (Figure 4A) and tandem repeat experiments (Figure 4B) in the HY box showed a decrease and a repeat number–dependent increase, respectively, of basal luciferase activity in human cells without RUNX-2 transfection. These indicate that the HY box may also function as a potent universal enhancer in the human COL10A1 promoter, responding to

various transcriptional stimulations besides RUNX-2 in human cells. Considering that chondrocyte hypertrophy is a crucial step for skeletal growth, repair, and OA progression, the HY box will be useful in the comprehensive screening of transcription factors or cofactors for COL10A1 transactivation and chondrocyte hypertrophy, which might be therapeutic targets for skeletal growth retardation, fractures, and OA.

ACKNOWLEDGMENTS

We thank Dr. Michael Owen (GlaxoSmithKline, London, UK) for providing Runx2$^{+/lacZ}$ mice. We also thank Reiko Yamaguchi and Hajime Kawahara for excellent technical assistance.

AUTHOR CONTRIBUTIONS

Dr. Kawaguchi had full access to all of the data in the study and takes responsibility for the integrity of the data and the accuracy of the data analysis.

Study design. Higashikawa, Saito, Ohba, Takeshita, Nakamura, Chung, Kawaguchi.

Acquisition of data. Higashikawa, Saito, Kamekura, Kan, Oshima.

Analysis and interpretation of data. Higashikawa, Ikeda, Ogata, Takeshita, Chung, Kawaguchi.

Manuscript preparation. Higashikawa, Takeshita, Kawaguchi.

Statistical analysis. Higashikawa, Saito, Kawamura, Kawaguchi.

REFERENCES

1. Kronenberg HM. Developmental regulation of the growth plate. Nature 2003;423:332–6.
2. Shapiro F. Bone development and its relation to fracture repair: the role of mesenchymal osteoblasts and surface osteoblasts. Eur Cell Mater 2008;15:53–76.
3. Von der Mark K, Kirsch T, Nerlich A, Kuss A, Weseloh G, Gluckert K, et al. Type X collagen synthesis in human osteoarthritic cartilage: indication of chondrocyte hypertrophy. Arthritis Rheum 1992;35:806–11.
4. Boos N, Nerlich AG, Wiest I, von der Mark K, Ganz R, Aebi M. Immunohistochemical analysis of type X-collagen expression in osteoarthritis of the hip joint. J Orthop Res 1999;17:495–502.
5. Kamekura S, Hoshi K, Shimoaka T, Chung U, Chikuda H, Yamada T, et al. Osteoarthritis development in novel experimental mouse models induced by knee joint instability. Osteoarthritis Cartilage 2005;13:632–41.
6. Linsenmayer TF, Long F, Nurminskaya M, Chen Q, Schmid TM. Type X collagen and other up-regulated components of the avian hypertrophic cartilage program. Prog Nucleic Acid Res Mol Biol 1998;60:79–109.
7. Rosati R, Horan GS, Pinero GJ, Garofalo S, Keene DR, Horton WA, et al. Normal long bone growth and development in type X collagen-null mice. Nat Genet 1994;8:129–35.
8. Kwan KM, Pang MK, Zhou S, Cowan SK, Kong RY, Pfordte T, et al. Abnormal compartmentalization of cartilage matrix components in mice lacking collagen X: implications for function. J Cell Biol 1997;136:459–71.
9. Jacenko O, Chan D, Franklin A, Ito S, Underhill CB, Bateman JF, et al. A dominant interference collagen X mutation disrupts hypertrophic chondrocyte pericellular matrix and glycosaminoglycan and proteoglycan distribution in transgenic mice. Am J Pathol 2001;159:2257–69.
10. Warman ML, Abbott M, Apte SS, Hefferon T, McIntosh I, Cohn DH, et al. A type X collagen mutation causes Schmid metaphyseal chondrodysplasia. Nat Genet 1993;5:79–82.
11. Wallis GA, Rash B, Sykes B, Bonaventure J, Maroteaux P, Zabel B, et al. Mutations within the gene encoding the α1 (X) chain of type X collagen (COL10A1) cause metaphyseal chondrodysplasia type Schmid but not several other forms of metaphyseal chondrodysplasia. J Med Genet 1996;33:450–7.
12. Chan D, Jacenko O. Phenotypic and biochemical consequences of collagen X mutations in mice and humans. Matrix Biol 1998;17:169–84.
13. Ducy P, Zhang R, Geoffroy V, Ridall AL, Karsenty G. Osf2/Cbfa1: a transcriptional activator of osteoblast differentiation. Cell 1997;89:747–54.
14. Komori T. Regulation of osteoblast differentiation by transcription factors. J Cell Biochem 2006;99:1233–9.
15. Kim IS, Otto F, Zabel B, Mundlos S. Regulation of chondrocyte differentiation by Cbfa1. Mech Dev 1999;80:159–70.
16. Inada M, Yasui T, Nomura S, Miyake S, Deguchi K, Himeno M, et al. Maturational disturbance of chondrocytes in Cbfa1-deficient mice. Dev Dyn 1999;214:279–90.
17. Enomoto H, Enomoto-Iwamoto M, Iwamoto M, Nomura S, Himeno M, Kitamura Y, et al. Cbfa1 is a positive regulatory factor in chondrocyte maturation. J Biol Chem 2000;275:8695–702.
18. Takeda S, Bonnamy JP, Owen MJ, Ducy P, Karsenty G. Continuous expression of Cbfa1 in nonhypertrophic chondrocytes uncovers its ability to induce hypertrophic chondrocyte differentiation and partially rescues Cbfa1-deficient mice. Genes Dev 2001;15:467–81.
19. Ueta C, Iwamoto M, Kanatani N, Yoshida C, Liu Y, Enomoto-Iwamoto M, et al. Skeletal malformations caused by overexpression of Cbfa1 or its dominant negative form in chondrocytes. J Cell Biol 2001;153:87–100.
20. Zheng Q, Zhou G, Morello R, Chen Y, Garcia-Rojas X, Lee B. Type X collagen gene regulation by Runx2 contributes directly to its hypertrophic chondrocyte-specific expression in vivo. J Cell Biol 2003;162:833–42.
21. Komori T. Requisite roles of Runx2 and Cbfb in skeletal development. J Bone Miner Metab 2003;21:193–7.
22. Kamekura S, Kawasaki Y, Hoshi K, Shimoaka T, Chikuda H, Maruyama Z, et al. Contribution of runt-related transcription factor 2 to the pathogenesis of osteoarthritis in mice after induction of knee joint instability. Arthritis Rheum 2006;54:2462–70.
23. Kawaguchi H. Endochondral ossification signals in cartilage degradation during osteoarthritis progression in experimental mouse models. Mol Cells 2008;25:1–6.
24. Kugimiya F, Kawaguchi H, Kamekura S, Chikuda H, Ohba S, Yano F, et al. Involvement of endogenous bone morphogenetic protein (BMP) 2 and BMP6 in bone formation. Calcif Tissue Int 2005;280:35704–12.
25. Yamada T, Kawano H, Koshizuka Y, Fukuda T, Yoshimura K, Kamekura S, et al. Carminerin contributes to chondrocyte calcification during endochondral ossification. Nat Med 2006;12:665–70.
26. Yamakawa K, Kamekura S, Kawamura N, Saegusa M, Kamei D, Murakami M, et al. Association of microsomal prostaglandin E synthase 1 deficiency with impaired fracture healing, but not with bone loss or osteoarthritis, in mouse models of skeletal disorders. Arthritis Rheum 2008;58:172–83.
27. Kitamura T. New experimental approaches in retrovirus-mediated expression screening. Int J Hematol 1998;67:351–9.
28. Morita S, Kojima T, Kitamura T. Plat-E: an efficient and stable system for transient packaging of retroviruses. Gene Ther 2000;7:1063–6.
29. Saito T, Ikeda T, Nakamura K, Chung UI, Kawaguchi H. S100A1

and S100B, transcriptional targets of SOX trio, inhibit terminal differentiation of chondrocytes. EMBO Rep 2007;8:504–9.
30. Magne D, Bluteau G, Faucheux C, Palmer G, Vignes-Colombeix C, Pilet P, et al. Phosphate is a specific signal for ATDC5 chondrocyte maturation and apoptosis-associated mineralization: possible implication of apoptosis in the regulation of endochondral ossification. J Bone Miner Res 2003;18:1430–42.
31. Altschul SF, Gish W, Miller W, Myers EW, Lipman DJ. Basic local alignment search tool. J Mol Biol 1990;215:403–10.
32. Otto F, Thornell AP, Crompton T, Denzel A, Gilmour KC, Rosewell IR, et al. Cbfa1, a candidate gene for cleidocranial dysplasia syndrome, is essential for osteoblast differentiation and bone development. Cell 1997;89:765–71.
33. Uchida H, Zhang J, Nimer SD. AML1A and AML1B can transactivate the human IL-3 promoter. J Immunol 1997;158:2251–8.
34. Mundlos S, Otto F, Mundlos C, Mulliken JB, Aylsworth AS, Albright S, et al. Mutations involving the transcription factor CBFA1 cause cleidocranial dysplasia. Cell 1997;89:773–9.
35. Otto F, Kanegane H, Mundlos S. Mutations in the RUNX2 gene in patients with cleidocranial dysplasia. Hum Mutat 2002;19:209–16.
36. Iwamoto M, Shimazu A, Pacifici M. Regulation of chondrocyte maturation by fibroblast growth factor-2 and parathyroid hormone. J Orthop Res 1995;13:838–45.
37. O'Keefe RJ, Loveys LS, Hicks DG, Reynolds PR, Crabb ID, Puzas JE, et al. Differential regulation of type-II and type-X collagen synthesis by parathyroid hormone-related protein in chick growth-plate chondrocytes. J Orthop Res 1997;15:162–74.
38. Riemer S, Gebhard S, Beier F, Poschl E, von der Mark K. Role of c-fos in the regulation of type X collagen gene expression by PTH and PTHrP: localization of a PTH/PTHrP-responsive region in the human COL10A1 enhancer. J Cell Biochem 2002;86:688–99.
39. Thomas JT, Sweetman WA, Cresswell CJ, Wallis GA, Grant ME, Boot-Handford RP. Sequence comparison of three mammalian type-X collagen promoters and preliminary functional analysis of the human promoter. Gene 1995;160:291–6.
40. Beier F, Vornehm S, Poschl E, von der Mark K, Lammi MJ. Localization of silencer and enhancer elements in the human type X collagen gene. J Cell Biochem 1997;66:210–8.
41. Chambers D, Young DA, Howard C, Thomas JT, Boam DS, Grant ME, et al. An enhancer complex confers both high-level and cell-specific expression of the human type X collagen gene. FEBS Lett 2002;531:505–8.
42. Gebhard S, Poschl E, Riemer S, Bauer E, Hattori T, Eberspaecher H, et al. A highly conserved enhancer in mammalian type X collagen genes drives high levels of tissue-specific expression in hypertrophic cartilage in vitro and in vivo. Matrix Biol 2004;23:309–22.

DOI 10.1002/art.24376

Errata

In the articles by Valdes et al in the January 2007 and February 2006 issues of *Arthritis & Rheumatism* (pages 137–146 and 533–539, respectively), some information on sample collection and a funding source was omitted. Collection of some of the samples used for genetic association was carried out by Andrew Carr, MD (Nuffield Orthopaedic Centre, Botnar Research Centre, Oxford University, Oxford, UK), and funding was provided by the Norman Collisson Foundation, the Botnar Foundation, and the Lord Nuffield Orthopaedic Trust).

We regret the errors.

SPINE Volume 34, Number 3, pp E110–E114

Radiographic Analysis of the Cervical Spine in Patients With Retro-Odontoid Pseudotumors

Hirotaka Chikuda, MD,* Atsushi Seichi, MD,† Katsushi Takeshita, MD,* Naoki Shoda, MD,* Takashi Ono, MD,* Ko Matsudaira, MD,* Hiroshi Kawaguchi, MD,* and Kozo Nakamura, MD*

Study Design. A retrospective review of 10 consecutive patients with a noninflammatory retro-odontoid pseudotumor.

Objective. To examine the radiographic characteristics in patients with a retro-odontoid pseudotumor and to evaluate the efficacy of posterior fusion.

Summary of Background Data. A retro-odontoid pseudotumor, a reactive fibrocartilaginous mass, is known to develop after chronic atlantoaxial instability; however, one-third of the reported cases showed no overt atlantoaxial instability. The pathomechanism for such "atypical" cases remains unclear, although altered cervical motion secondary to ossification of the anterior longitudinal ligament (OALL) or severe spondylosis has been implicated.

Methods. We reviewed the charts and radiographs of 10 patients with a retro-odontoid pseudotumor who underwent surgery. Preoperative radiographs were evaluated for atlas-dens interval (ADI), presence of OALL, range of motion, and segmental motion adjacent to the atlantoaxial joint. Computed tomography was evaluated for degenerative changes of zygapophysial joints.

Results. There were 6 men and 4 women. Atlantoaxial instability (ADI >4 mm) was observed in 2 patients. ADI was less than 3 mm in 5 patients. Frequent association of OALL (6 patients) and marked decrease in C2 to C7 range of motion (mean, 17.6°; range, 3°–36°) were noted. Ankylosis of O-C1 was observed in 4 patients and C2 to C3 in 6. Severe degenerative change of C2 to C3 zygapophysial joint was observed in 4 patients. The patients underwent occipito-cervical fusion (9 patients) or direct removal of the pseudotumor (1 patient). Postoperative magnetic resonance imaging invariably demonstrated the mass regression.

Conclusion. Retro-odontoid pseudotumors were not always associated with radiographic atlantoaxial instability. Our data indicate that extensive OALL and ankylosis of the adjacent segments are risk factors for the formation of the pseudotumor. Retro-odontoid pseudotumors may develop as an "adjacent segment disease" after altered biomechanics of the cervical spine, especially those in the adjacent segments. Posterior fusion was effective even in cases without radiographic atlantoaxial instability.

Key words: retro-odontoid pseudotumor, atlantoaxial joint, adjacent segment, ossification of the anterior ligament, hyperostosis, myelopathy, range of motion, spinal fusion. **Spine 2009;34:E110–E114**

A noninflammatory retro-odontoid pseudotumor is a reactive fibrocartilaginous mass formed posterior to the odontoid process.[1–3] The retro-odontoid pseudotumor, a rare but increasingly recognized clinical entity, reportedly develops subsequent to chronic atlantoaxial instability. This view has been further supported by the regression of the mass after posterior fusion, which has become the mainstay of the treatment.[4–9] Although retro-odontoid pseudotumors have been frequently associated with atlantoaxial subluxation, we found that about one-third of the cases reported in the literature showed no overt atlantoaxial instability.[2,5,6,9–14] The pathomechanism for such atypical cases remains unclear, although modified stress distribution of the cervical spine, secondary to severe spondylosis or OALL, has been implicated.[15,16] Moreover, it has not been clarified whether posterior fusion aiming at spontaneous mass regression is similarly effective for the patients without radiographic atlantoaxial instability.

To further elucidate the underlying pathomechanism of the disease, we examined the radiographic characteristics of the cervical spine in patients with the retro-odontoid pseudotumors. Special attention was paid to the presence of OALL and the segmental motion adjacent to the atlantoaxial joint (O-C1, C2–C3). We also evaluated the efficacy of posterior fusion surgery.

Materials and Methods

After approval of institutional review board, we reviewed the clinical records of 140 patients who underwent surgery for upper cervical lesion at our department between 2000 and 2006. We identified 10 patients with retro-odontoid pseudotumors, and the radiographs of the 10 patients were examined. The diagnosis was made based primarily on magnetic resonance imaging (MRI) that revealed a mass lesion posterior to the odontoid process with substantial cord compression as evidenced by effacement of the subarachnoid space and indentation of the spinal cord. Masses were typically visualized as ranging from isointense to hypointense relative to spinal cord tissue on T1-weighted images and as hypointense regions on T2-weighted images. The diagnosis

From the *Department of Orthopaedic Surgery, Faculty of Medicine, the University of Tokyo, Tokyo, Japan; and †Department of Orthopaedic Surgery, Jichi Medical University, Jichi, Japan.
Acknowledgment date: March 27, 2008. Revision date: July 08, 2008. Acceptance date: July 21, 2008.
The manuscript submitted does not contain information about medical device(s)/drug(s).
No funds were received in support of this work. No benefits in any form have been or will be received from a commercial party related directly or indirectly to the subject of this manuscript.
This study was approved by the Tokyo University Medical Research Ethics Committee.
Address correspondence and reprint requests to Hirotaka Chikuda, MD, Department of Orthopaedic Surgery, Faculty of Medicine, the University of Tokyo, 7–3–1 Hongo, Bunkyo-ku, Tokyo 113-8655, Japan; E-mail: chikuda-tky@umin.ac.jp

Table 1. Scores of the Motor Functions of the Upper and Lower Extremities for Cervical Myelopathy Set by the Japanese Orthopaedic Association (JOA)

Motor function of the upper extremities (upper m-JOA)	
0	Cannot eat with a spoon
1	Can eat with a spoon, but not with chopsticks
2	Can eat with chopsticks, but to a limited degree
3	Can eat with chopsticks, but awkward
4	No disability
Motor function of the lower extremities (lower m-JOA)	
0	Cannot walk
1	Needs cane or aid on flat ground
2	Needs cane or aid only on stairs
3	Can walk without cane or aid, but slowly
4	No disability

was further confirmed by the radiology report. Specimen of the mass was available in 2 patients (patient 1 and 2). Subsequent histologic examination revealed fibrocartilage and degenerative ligamentous tissue. There was no recurrence of the mass lesion during the follow-up period. Inflammatory granulation of the synovium associated with rheumatoid arthritis and retro-odontoid reactive lesions associated with pseudarthrosis of the dens fracture were excluded from this study. All patients had symptoms of progressive myelopathy: hyperreflexia, positive pathologic reflexes, motor weakness in the upper and lower extremities, clumsiness in hands, and gait disturbance. Neurologic status of the patients was evaluated before surgery and at the last follow-up by a senior author (A.S.). Motor function was rated using the motor function scores of the upper and lower extremities for cervical myelopathy set by the Japanese Orthopedic Association (upper and lower m-JOA score) (Table 1). A full score "4" indicates normal function.

All radiographs were viewed using our institution's digital radiography software (Centricity Web-J software ver.1.6.11; GE Yokogawa Medical Systems, Tokyo, Japan). The measurement of the radiographs was performed independently by 2 spine surgeons (H.C. and N.S.) with the program's digital measuring tool. The results of the 2 reviewers were averaged. The atlas-dens interval (ADI) was measured on preoperative flexion-extension radiographs. The atlantoaxial instability was defined as ADI >4 mm, according to the criteria described by White and Panjabi.[17] Lateral radiographs and sagittal computed tomography (CT) reconstructions were evaluated for the presence of OALL. OALL was defined as bony mass anterior to the vertebrae bridging over 2 or more intervertebral disc spaces. Range of motion (ROM) was measured on preoperative flexion-extension radiographs. The representative lines used for the measurement were as follows: the McGregor line, the line passing through the centers of anterior and posterior arches of the atlas, and the line parallel to the endplate of vertebrae. The mobility of each segment was determined by measuring the difference between 2 corresponding points on the tips of the spinous processes on flexion *versus* extension. Ankylosis was defined as absence of motion on both flexion and extension radiographs. CT reconstructions were further evaluated for degenerative change or fusion of the zygapophysial joints. To assess the regression of the pseudotumor, follow-up MRI obtained 1 year after surgery was reviewed. Maximal thickness of the retro-odontoid soft tissue was measured on preoperative and postoperative MRI in T2-weighted sagittal view. Interobserver reliability of radiographic measurement was assessed with inter class coefficient. All statistics were calculated using SPSS, version 13.0 (SPSS Inc., Chicago, IL).

■ Results

There were 6 men and 4 women with a mean age at surgery of 71 years (range, 58–82 years). Mean follow-up was 30 months (range, 12–84 months). Maximal thickness of the retro-odontoid soft tissue was 9.4 ± 1.3 mm (mean ± SD; range, 7.6-11.4 mm). On examination of the radiographic characteristics (Table 2), ADI averaged 3.4 ± 1.9 mm (mean ± SD) in flexion and 1.8 ± 0.9 mm in extension. Only 2 patients showed overt atlantoaxial instability (ADI >4 mm). ADI was less than 3 mm in 5 patients (Figure 1). We found extensive OALL in 6 patients: C2 to C7 in 4 patients, and C3 to C7 and C3 to C5 in 1 patient each. When ROM of the cervical spine was examined, marked decrease in subaxial (C2–C7)

Table 2. Radiographic Characteristics of the Cervical Spine

		ADI (mm)			ROM (°)		Segmental Motion (°)	
Patient No.	Age (Yr), Sex	Flexion	Extension	OALL	O-C2	C2–C7	O-C1	C2–C3
1	58, M	7.0 ± 0.1	3.2 ± 0.3	C2–C7	30 ± 3.0	6 ± 1.5	7 ± 1.0	10 ± 3.0
2	67, F	6.6 ± 0.6	6.2 ± 0	C3–C5	14 ± 9.1	28 ± 3.9	None*	None
3	72, F	3.5 ± 0.7	1.0 ± 0.1	C2–C7	32 ± 0.9	7 ± 0.6	6 ± 1.1	8 ± 3.6
4	71, M	3.4 ± 0.1	1.5 ± 0	—	17 ± 0.4	23 ± 0.7	None	3 ± 0.2
5	82, M	3.3 ± 0.4	2.1 ± 0.3	C2–C7	18 ± 5.3	5 ± 4.9	8 ± 0.1	None
6	81, M	2.8 ± 0.6	1.5 ± 1.0	C2–C7	35 ± 1.7	22 ± 2.6	5 ± 0.8	None†
7	73, F	2.7 ± 0.1	1.9 ± 0.4	—	24 ± 1.1	35 ± 0.2	None	5 ± 2.5†
8	73, M	2.0 ± 0.6	1.7 ± 0.3	C3–C7	8 ± 0.3	11 ± 2.4	None	None†
9	71, F	2.0 ± 0.3	1.7 ± 0.9	—	28 ± 6.2	36 ± 2.8	4 ± 1.6	None
10	64, M	1.0 ± 0.1	0 ± 0	—	24 ± 2.7	3 ± 3.5	15 ± 3.1	None†

Data are shown as mean ± SD. ICC values for radiographic measurement were as follows: ADI in flexion, 0.97; ADI in extension, 0.98; O-C2 ROM, 0.88; C2–C7 ROM, 0.98; O-C1 ROM, 0.96; and C2–C3 ROM, 0.87. The 2 reviewers were in accord regarding the categorical items including presence of OALL and segmental ankylosis.
*Atlanto-occipital assimilation.
†Severe spondylosis of the C2–C3 zygapophyseal joint.

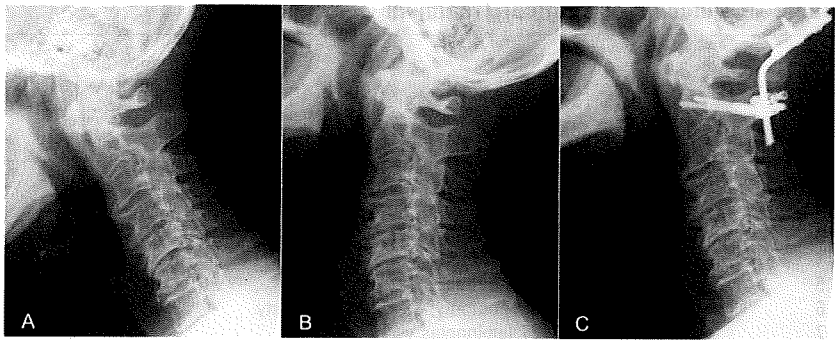

Figure 1. Preoperative radiographs of a 73-year-old man (patient 8) revealed extensive OALL. Atlantoaxial instability was not evident in flexion (**A**) and extension (**B**). The patient underwent O-C2 fusion with C1 laminectomy (**C**).

ROM was noted (mean, 17.6°; range, 3°-36°), especially in the patients with OALL. Further analysis of the segmental motion revealed ankylosis in O-C1 in 4 patients (including 1 patient with atlanto-occipital assimilation) and C2–C3 in 6 patients. Furthermore, CT revealed severe degenerative changes of the C2 to C3 zygapophysial joint in 4 patients (Figure 2).

All but 1 patient were treated with posterior occipitocervical fusion using pedicle screws (Table 3). Surgical procedures included O-C2 fusion (6 patients), O-C4 fusion(3 patients), and direct tumor resection by the lateral approach(1 patient). Additional C1 laminectomy was performed in all patients who underwent posterior fusion except 1 patient in whom adequate decompression was confirmed with intraoperative ultrasonography. There was no documented complication during perioperative period except that 1 patient had acute coronary syndrome, which required subsequent intervention. Neurologic status improved after surgery in all but 1 patient who was suffering from esophageal cancer. Preoperative upper m-JOA score (median, 2; range, 1–3) improved after surgery (median, 3.5; range, 1–4). Similarly, lower m-JOA score (median, 2; range, 1–3) also improved after surgery (median, 3; range, 2–4). Follow-up MRI was available in 8 patients. In the remaining 2 patients, deteriorated health status due to unrelated diseases (esophageal cancer and pneumonia, respectively) precluded further study. MRI revealed the regression of the pseudotumors in all patients and decompression of the spinal cord (Figure 3). Regression of the pseudotumors was confirmed by emergence of the subarachnoid space in postoperative MRI and further evidenced by reduction in thickness of the retro-odontoid soft tissue (3.4 ± 0.8 mm; range, 2.3-4.7 mm).

■ Discussion

Our study had 3 main findings. First, we have shown that the retro-odontoid pseudotumors can develop without overt atlantoaxial instability. Second, we found marked decrease in subaxial ROM, mainly because of extensive OALL. Furthermore, most of the patients had ankylosis of O-C1 or C2 to C3, the segments adjacent to the atlantoaxial joint. Finally, spontaneous mass regression occurred after posterior fusion even in the absence of radiographic atlantoaxial instability.

The retro-odontoid pseudotumor has been generally considered as a rare sequela of atlantoaxial subluxation. In the postulated view on its pathomechanism, preexisting atlantoaxial instability was presumed to cause repeated tear and subsequent hypertrophy of the transverse ligament,[4,16] thus leading to the formation of the pseudotumor. The current study, however, revealed that the retro-odontoid pseudotumors were not necessarily associated with overt atlantoaxial instability. This finding indicates a different view on the formation of the pseudotumor: In the first place, excessive stress concentration to the atlantoaxial complex, due to altered biomechanics of the cervical spine, may repeatedly cause damage to the transverse ligament. A reactive mass may develop gradually after cycles of repetitive injuries to the ligament and reparative process. Although atlantoaxial subluxation might ensue from further attenuation of the

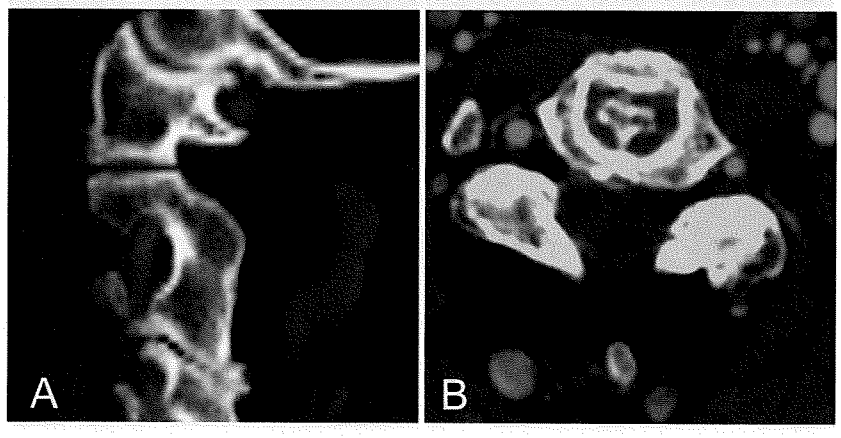

Figure 2. Sagittal (**A**) and axial (**B**) CT reconstructions (both from patient 8) demonstrated severe spondylosis in bilateral C2 to C3 zygapophysial joints.

Table 3. Outcome of Surgical Treatment

Patient No.	Surgery	Preoperative m-JOA		Postoperative m-JOA		Outcome	Follow-up MRI
		Upper	Lower	Upper	Lower		
1	Partial removal, O-C2 fusion, C1 laminectomy	1	1	2	2	Improved	Regression
2	Direct removal	2	1	4	4	Improved	Extirpated
3	O-C4 fusion, C1 laminectomy	1	2	3	3	Improved	N.A.*
4	O-C2 fusion, C1 laminectomy	1	2	3	3	Improved	Regression
5	O-C4 fusion, C1 laminectomy	1	2	1	2	Unchanged	N.A.*
6	O-C2 fusion, C1 laminectomy, C3–C7 laminoplasty	2	2	3	2	Improved	Regression
7	O-C2 fusion, C3–C7 laminoplasty	3	2	4	4	Improved	Regression
8	O-C2 fusion, C1 laminectomy	3	3	4	4	Improved	Regression
9	O-C2 fusion, C1 laminectomy	2	2	4	4	Improved	Regression
10	O-C4 fusion, C1–C2 laminectomy	2	2	4	3	Improved	Regression

*Deterioration of the patient's condition due to unrelated diseases precluded the follow-up MRI study.
Upper, indicates upper extremities; Lower, lower extremities; N.A., not available.

ligamentous structure, atlantoaxial instability should be viewed as a consequence of the degeneration process, not a prerequisite for the formation of the pseudotumor.

We found that extensive OALL was highly prevalent in patients with retro-odontoid pseudotumors. Modified stress distribution secondary to extensive OALL has been implicated in the literature as possible pathomechanism. Jun *et al* reported a case with diffuse idiopathic skeletal hyperostosis and attributed its cause to loss of mobility of subaxial segments and the secondary transfer of mechanical stress to the atlantoaxial segment.[16] Patel *et al* reported 5 patients of a retro-odontoid mass associated with Forestier disease, speculating that multilevel subaxial fusion because of OALL coupled with the mobility of the craniovertebral joint complex plays a pivotal role in the development of the mass.[15] In line with these reports, the current study demonstrated extensive OALL and marked decrease in subaxial ROM in patients with a retro-odontoid pseudotumor. Our data indicate that altered biomechanics of the cervical spine because of OALL plays a role in formation of the retro-odontoid pseudotumor.

Ankylosis of the segments adjacent to the atlantoaxial joint was another characteristic finding associated with retro-odontoid pseudotumors. Loss of mobility at the adjacent segment is known to contribute to increased risk of atlantoaxial dysfunction in other chronic condi-

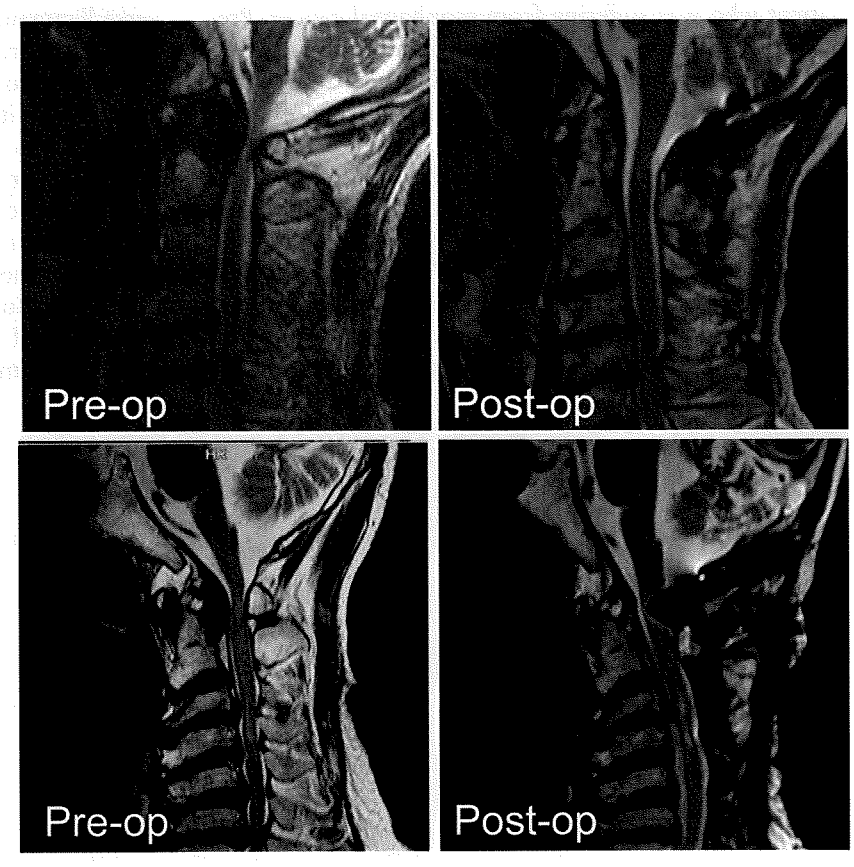

Figure 3. Preoperative and postoperative T2-weighted MR images of patient 8 (upper panels) and patient 6 (lower panels). Spontaneous regression of the mass lesion occurred after posterior fusion.

tions. In patients with Klippel-Feil syndrome, in which the C2 to C3 is the most commonly fused level, subsequent stress transfer at the C1 to C2 segment has been suggested as a risk factor for atlantoaxial instability. Shen *et al* have shown that occipitalization combined with a fused C2 to C3 segment results in the greatest amount of atlantoaxial instability in patients with Klippel-Feil syndrome.[18] Our results suggest that the altered dynamics of the cervical spine, especially those in the adjacent segments —O-C1 and C2 to C3—play a crucial role in the development of the retro-odontoid pseudotumor, indicating that the mass develops as an adjacent segment disease.

Optimal treatment for a retro-odontoid pseudotumor that is not associated with atlantoaxial instability has not been established, although transoral removal has usually been employed in such a case. In this study, 3 types of surgical procedures were used: extirpation of the mass, O-C2 fusion, and O-C4 fusion. We performed extirpation only in the earlier period when posterior fusion was not known to be effective. Afterward, we used posterior fusion as the treatment of choice. We preferred occipito-cervical fusion to C1 to C2 fusion because of ample space for bone grafting even after the resection of C1 posterior arch, which was performed in most cases. We usually extended fusion down to C4 when safety of inserting C2 pedicle screws was in doubt because of the anatomic limitations such as high riding vertebral artery, identified by preoperative planning using CT navigation system. In the current study, we have shown that posterior fusion invariably produced mass regression even in cases without radiographic atlantoaxial instability. This previously undocumented finding may be attributable to the fact that posterior fusion greatly reduces stress concentration to the atlantoaxial junction. Considering that the reactive mass develops as an adjacent segment disease, relieving mechanical stress at the atlantoaxial junction is a reasonable strategy for preventing further progression of the disease. Our data indicate that posterior fusion is the treatment of choice even for cases without overt atlantoaxial instability.

There are several limitations to the present study. Although this is the largest case series, we need to examine more cases to determine the precise incidence of the radiographic characteristics we mentioned. Moreover, a cohort or case-control study is required to further demonstrate the cause-effect relationship of the putative risk factors we discussed in the present study. Retro-odontoid pseudotumors occur only in a fraction of population with OALL or having ankylosis of O-C1 or C2 to C3, which may be partly attributable to variable biologic responses of the ligamentous tissue among the individuals. Further studies are needed to clarify the role of other biologic or genetic factors that predispose patients to development of retro-odontoid pseudotumors.

■ Conclusion

Retro-odontoid pseudotumors were not always associated with radiographic atlantoaxial instability. Our results suggest that extensive OALL and ankylosis of the adjacent segments are risk factors for the formation of pseudotumors. The retro-odontoid pseudotumors may develop as an adjacent segment disease after altered biomechanics of the cervical spine, especially those in the adjacent segments. Posterior fusion is the treatment of choice even for cases without radiographic atlantoaxial instability.

■ Key Points

- Retro-odontoid pseudotumors were not necessarily associated with radiographic atlantoaxial instability.
- Subaxial fusion due to OALL and ankylosis of the adjacent segments (O-C1, C2–C3) may be risk factors for the formation of the pseudotumor.
- Posterior fusion resulted in spontaneous regression of the pseudotumor even in cases without radiographic atlantoaxial instability.

References

1. Oohori Y, Seichi A, Kawaguchi H, et al. Retroodontoid pseudotumor resected by a high cervical lateral approach in a rheumatoid arthritis patient: a case report. *J Orthop Sci* 2004;9:90–3.
2. Crockard HA, Sett P, Geddes JF, et al. Damaged ligaments at the craniocervical junction presenting as an extradural tumour: a differential diagnosis in the elderly. *J Neurol Neurosurg Psychiatr* 1991;54:817–21.
3. Sze G, Brant-Zawadzki MN, Wilson CR, et al. Pseudotumor of the craniovertebral junction associated with chronic subluxation: MR imaging studies. *Radiology* 1986;161:391–4.
4. Yoshida MT, Kawakami M, Natsumi K, et al. Retro-odontoid pseudotumor associated with chronic atlanto-axial instability. *Rinsho Seikei Geka* 1995; 30:395–402 [in Japanese].
5. Yamashita K, Aoki Y, Hiroshima K. Myelopathy due to hypoplasia of the atlas: a case report. *Clin Orthop Relat Res* 1997:90–3.
6. Yamaguchi I, Shibuya S, Arima N, et al. Remarkable reduction or disappearance of retroodontoid pseudotumors after occipitocervical fusion: report of three cases. *J Neurosurg Spine* 2006;5:156–60.
7. Jun BY. Complete reduction of retro-odontoid soft tissue mass in os odontoideum following the posterior C1–C2 tranarticular screw fixation. *Spine* 1999;24:1961–4.
8. Lagares A, Arrese I, Pascual B, et al. Pannus resolution after occipitocervical fusion in a non-rheumatoid atlanto-axial instability. *Eur Spine J* 2006;15: 366–9.
9. Lansen TA, Kasoff SS, Tenner MS. Occipitocervical fusion for reduction of traumatic periodontoid hypertrophic cicatrix: case report. *J Neurosurg* 1990;73:466–70.
10. Rabadan AT, Sevlever G. Hypertrophic atlantoaxial ligaments: an unusual cause of compression of the upper spinal cord. *J Neurol Neurosurg Psychiatr* 2000;68:116–17.
11. Komatsu Y, Shibata T, Yasuda S, et al. Atlas hypoplasia as a cause of high cervical myelopathy: case report. *J Neurosurg* 1993;79:917–19.
12. Chen TY, Lui TN. Retrodental fibrocartilaginous mass: report of a case. *Spine* 1997;22:920–3.
13. Sato K, Kubota T, Takeuchi H, et al. Atlas hypoplasia associated with non-traumatic retro-odontoid mass. *Neurol Med Chir (Tokyo)* 2006;46:202–5.
14. Suetsuna F, Narita H, Ono A, et al. Regression of retroodontoid pseudotumors following C-1 laminoplasty: report of three cases. *J Neurosurg Spine* 2006;5:455–60.
15. Patel NP, Wright NM, Choi WW, et al. Forestier disease associated with a retroodontoid mass causing cervicomedullary compression. *J Neurosurg* 2002;96:190–6.
16. Jun BY, Yoon KJ, Crockard A. Retro-odontoid pseudotumor in diffuse idiopathic skeletal hyperostosis. *Spine* 2002;27:E266–70.
17. White AA, Panjabi, MM. *Clinical Biomechanics of the Spine.* 2nd ed. Philadelphia: Lippincott Williams and Wilkins; 1990.
18. Shen FH, Samartzis D, Herman J, et al. Radiographic assessment of segmental motion at the atlantoaxial junction in the Klippel-Feil patient. *Spine* 2006;31:171–7.

Biomaterials 30 (2009) 5201–5208

Contents lists available at ScienceDirect

Biomaterials

journal homepage: www.elsevier.com/locate/biomaterials

Controlled drug release from multilayered phospholipid polymer hydrogel on titanium alloy surface

Jiyeon Choi [a,c], Tomohiro Konno [b,c], Madoka Takai [a,c], Kazuhiko Ishihara [a,b,c,*]

[a] Department of Materials Engineering, School of Engineering, The University of Tokyo, 7-3-1, Hongo, Bunkyo-ku, Tokyo 113-8656, Japan
[b] Department of Bioengineering, School of Engineering, The University of Tokyo, 7-3-1, Hongo, Bunkyo-ku, Tokyo 113-8656, Japan
[c] Center for NanoBio Integration, The University of Tokyo, 7-3-1, Hongo, Bunkyo-ku, Tokyo 113-8656, Japan

ARTICLE INFO

Article history:
Received 16 April 2009
Accepted 2 June 2009
Available online 27 June 2009

Keywords:
Layer-by-layer self-assembly
Multilayer
Hydrogel
Paclitaxel
Controlled release

ABSTRACT

Here we describe the functionalization of a multilayered hydrogel layer on a Ti alloy with an anti-neoplastic agent, paclitaxel (PTX). The multilayered hydrogel was synthesized via layer-by-layer self-assembly (LbL) using selective intermolecular reactions between two water-soluble polymers, phospholipid polymer (PMBV) containing a phenylboronic acid unit and poly(vinyl alcohol) (PVA). Reversible covalent bonding between phenylboronic acid and the polyol provided the driving force for self-assembly. Poorly water-soluble PTX dissolves in PMBV aqueous solutions because PMBV is amphiphilic. Therefore, our multilayered hydrogel could be loaded with PTX at different locations to control the release profile and act as a drug reservoir. The amount of PTX incorporated in the hydrogel samples increased with the number of layers but was not directly proportional to the number of layers. However, as the step for making layers was repeated, the concentration of PTX in the PMBV layers increased. The different solubilities of PTX in PMBV and PVA aqueous solutions allow for the production of multilayered hydrogels loaded with PTX at different locations. In vitro experiments demonstrated that the location of PTX in the multilayered hydrogel influences the start and profile of PTX release. We expect that this rapid and facile LbL synthesis of multilayered hydrogels and technique for in situ loading with PTX, where the location of loading controls the release pattern, will find applications in biomedicine and pharmaceutics as a promising new technique.

1. Introduction

There has been significant progress recently in the use of implantable biomedical devices such as the cardiovascular stent [1,2], artificial blood pump [3], biosensor [4,5], and artificial joint [6,7]. Developments in the use of polymeric biomaterials associated with drug therapies for improved therapeutic effects can be exploited in a wide variety of applications. Moreover, when drug-releasing agents are applied on to specific implant surfaces, they offer a means of local drug delivery. This allows for high regional drug concentrations with prolonged retention at lower doses and the direct delivery of agents with short half-lives, such as proteins and peptides, to a site with minimal loss. Consequently, there is a reduction in systemic toxicity and an improvement in patient compliance [8,9]. The various approaches include embedding drugs in polymers such as stimuli-sensitive hydrogels that are triggered to release the drugs by changes in environmental factors such as pH [10,11], ionic strength [12], temperature [13], magnetic fields [14], or any combination of these [15].

The layer-by-layer self-assembly (LbL) method using a polyelectrolyte has attracted considerable interest owing to its flexibility in terms of the choice of assembly components and ease of processing [16–26]. This technique allows nanoscale control over the deposition of a large variety of functional materials, which are polymer layers assembled by taking advantage of attractive interactions such as electrostatic interactions, covalent bonding, and hydrogen bonding [17–19]. Recently, the LbL method has been used in developing a drug delivery system for the sustained and controlled release of incorporated molecules [20,21]. In most such research, multilayered coatings are used for their structural properties by dissociation of polymer layers. They can be loaded with bioactive molecules through simple adsorption by dipping a film in a solution containing the bioactive molecules [22–24]. Different loading modalities are possible; it is possible to incorporate bioactive agents within a multilayered structure by the LbL method [25,26]. In this study, we propose a multilayered hydrogel capable

* Corresponding author. Department of Materials Engineering, School of Engineering, The University of Tokyo, 7-3-1, Hongo, Bunkyo-ku, Tokyo 113-8656, Japan. Tel.: +81 3 5841 7142; fax: +81 3 5841 8647.
E-mail address: ishihara@mpc.t.u-tokyo.ac.jp (K. Ishihara).

0142-9612/$ – see front matter © 2009 Elsevier Ltd. All rights reserved.
doi:10.1016/j.biomaterials.2009.06.003

of the controlled release of bioactive agents depending on the location of the drug-loaded layer. We paclitaxel (PTX) as the bioactive agent for this study. PTX, extracted from the bark of the Pacific yew tree (*Taxus brevifolia*), has been used as a microtubule-stabilizing agent with potent antiproliferative activity [27]. However, its successful clinical application has been mainly limited by its low solubility in water and in addition, in the case of the commercially available PTX formulation, Taxol®, consisted in a mixture of Cremophor EL (polyoxyethylated castor oil) and absolute ethanol (50/50), it has been reported that additive agents for dissolving PTX cause serious side effects associated with hypersensitivity [28].

First, we synthesized a phospholipid polymer (PMBV) with 2-methacryloyloxyethyl phosphorylcholine (MPC), *n*-butyl methacrylate (BMA), and 4-vinylphenylboronic acid units (VPBA). MPC polymers have a phosphorylcholine (PC) group, which is a polar group also found on living cell membranes, and hence performs better than most other types of polymeric materials with respect to biocompatibility, which means the suppression of nonspecific protein adsorption [29–33]. In addition, they can be synthesized by random copolymerization between MPC and alkyl methacrylates [34]. For these reasons, MPC polymers are currently widely used in biomedical devices, including implantable artificial organs [6,7,35–38]. The phenylboronic acid moiety in PMBV allows the formation of a hydrogel with a polyol such as poly(vinyl alcohol) (PVA) [39]. Thus, PMBV and PVA can be used to synthesize PMBV/PVA multilayered hydrogel coatings via the LbL method [40]. Moreover, the BMA unit in PMBV induces the formation of hydrophobic domains in aqueous environments. For example, it has been reported that amphiphilic water-soluble MPC polymers such as poly(MPC-*co*-BMA) with a BMA mole fraction of 0.70 (PMB30W) form aggregate hydrophobic domains in aqueous environments, thus allowing PTX to dissolve in the aqueous polymer solution [41–43]. In the current study, we attempted to test whether the same possibilities existed with PMBV; that is, that it would have stable solubility against PTX in aqueous solution.

Here we report a multilayered phospholipid polymeric hydrogel that smartly incorporates PTX from solution during the construction of the multilayer via the LbL method. The use of multilayered hydrogels containing PC groups as surface modification agents has been explored for improving biocompatibility through increased resistance to protein adsorption [44,45] as well as for gene delivery by exploiting the electrostatic interaction between PC copolymers and DNA [46]. However, to the best of our knowledge, the present study is the first to introduce a direct PTX-loaded layer into a multilayered hydrogel bearing PC groups by means of the LbL method and to use such a hydrogel for controlled drug release.

The purpose of this study is to develop a multilayered phospholipid polymer hydrogel capable of the controlled release of bioactive agents (here, PTX) for localized drug delivery to numerous biomedical devices with metal substrates. We hypothesize that the location of the drug-loaded layer will influence the release profile. This study focuses on the functionality of PMBV/PVA as a drug reservoir and two types (referred to as the top and bottom types) of PTX-loaded PMBV/PVA multilayered hydrogels that are produced via the LbL method.

2. Materials and experimental methods

2.1. Materials

MPC was obtained from NOF Corporation (Tokyo, Japan); it was synthesized using a method developed by Ishihara et al. [47]. BMA was purchased from Nacalai Tesque Co. Ltd. (Tokyo, Japan). VPBA, PVA (degree of polymerization of 1500) and PTX were purchased from Wako Pure Chemical Industries Ltd. (Osaka, Japan). Octadecyltriethoxysilane (ODS) was purchased from ShinEtsu Chemical Co. Ltd. (Tokyo, Japan). Photoreactive PVA (azide-unit pendant water-soluble photopolymer; AWP) was purchased from Toyo Gosei Co. Ltd., Japan. Ti alloy substrates were obtained from Denisply-Sankin KK (Tokyo, Japan). Sodium 1-anilino-8-naphthalene sulfonate (ANS) was purchased from Tokyo Kasei Kogyo Co. Ltd. (Tokyo, Japan) and 1-pyrenylmethylmethacrylate (PMM) was purchased from Polyscience Inc. (Warrington, UK). Other reagents and solvents were of extra-pure grade and used without further purification. The synthesized phospholipid polymer PMBV was characterized by ^{1}H-nuclear magnetic resonance imaging, Fourier-transform infrared spectroscopy, and gel permeation chromatography. The molar fractions of monomers MPC, BMA, and VPBA were determined as 0.60:0.30:0.10 and those of the monomer units in the synthesized PMBV as 0.57:0.25:0.18, respectively. Also polymerization of MPC, BMA, VPBA and PMM carried out by the same procedure of PMBV case. The results are summarized in Table 1.

2.2. Evaluation of PMBV aggregation in aqueous solution

ANS was used to evaluate the polarity of the hydrophobic domain inside PMBV polymer aggregates. PMBV was directly dissolved in 1.0×10^{-5} M ANS aqueous solution and the concentration of PMBV was adjusted with the ANS aqueous solution. The internal polarity of the polymer aggregates was evaluated from the maximum wavelength in the fluorescence spectrum of ANS (excitation wavelength λ_{ex} of 350 nm, emission wavelength λ_{em} of 480 nm). The fluorescence spectrum was recorded with an FP-750 fluorescence spectrophotometer (Jasco, Tokyo, Japan).

2.3. Solubilization of PTX with polymer solutions

PTX (1 mg/mL) was dissolved in ethanol, and PMBV and PVA were dissolved in deionized water separately with polymer concentrations of 50 and 25 mg/mL, respectively. Then, a PTX-loaded PMBV solution was prepared by vortexing a mixture of the PTX and PMBV solutions in the ratio PMBV:PTX = 9:1 and then removing the ethanol under reduced pressure. A PTX-loaded PVA solution was also prepared in the same way. The undissolved PTX was sedimented by centrifugation at 10,300 rpm for 1 h. The supernatant was collected and the concentration of PTX in it was determined by high-performance liquid chromatography (HPLC; Tosoh System, Tokyo, Japan) with an ultraviolet (UV) detector. The conditions for the analysis were as follows: the mobile phase was a mixture of 50 wt% acetonitrile and methanol, the flow rate was 0.5 mL/min, the column was a C18 column, and the detection wavelength for the UV detector was 229 nm. A PMBV film containing PTX was made by evaporating the solvent from the previously mentioned solutions under a fume hood at room temperature for 3 d.

2.4. Preparation of multilayered hydrogel on Ti substrate

The procedure for the preparation of the multilayered hydrogel from PMBV and PVA has been reported previously [40]. Briefly, a Ti substrate was treated with ODS in toluene at 80 °C for 24 h. It was then coated with an aqueous solution of AWP (1 wt%) using the dip coating technique. Several such AWP-coated substrates were then air-dried under a fume hood at room temperature. They were then irradiated for 40 s with UV light (135 mW/cm^2) using a UV Spot Cure (SP-7, Ushio Inc., Yokohama, Japan).

PMBV solutions with concentrations of 50 and 25 mg/mL and a PVA solution with a concentration of 15 mg/mL were prepared from distilled water. Two combinations of PMBV and PVA solutions were examined: 50 mg/mL PMBV and 15 mg/mL PVA (PMBV50/PVA15) and 25 mg/mL PMBV and 15 mg/mL PVA (PMBV25/PVA15). Multilayer construction was accomplished by alternately dipping AWP-coated Ti substrates in PMBV and PVA solutions for 10 min each and subsequently rinsing with distilled water for 1 min. Six layers (three bilayers) were built by this LbL method, with PMBV constituting the outermost layer.

2.5. Determination of amount of PTX in the multilayered hydrogel

To 1 mg of PTX dissolved in 1 mL of ethanol was added PTX solution to the prescribed concentration ratio PTX:PMBV = 1:9; the ethanol was subsequently evaporated under reduced pressure. Multiple layers were constructed as mentioned above. To determine the amount of PTX in the hydrogel layer, the PTX in the sample

Table 1
Characteristics of the fluorescence-labeled PMBV (PMBVP).

Abb.	Monomer unit fraction[a]		Molecular weight, Mw ($\times 10^4$)[b]
	In feed	In polymer	
	MPC/BMA/VPBA/PMM	MPC/BMA/VPBA/PMM	
PMBVP	0.600/0.299/0.100/0.01	0.607/0.296/0.091/0.006	6.2

$[\text{Monomer}]_{total}$ = 1 mol/L in EtOH; [AIBN] = 1 mmol/L.
Copolymerization time: 2.5 h, polymerization temperature: 60 °C.
[a] Determined by ^{1}H NMR.
[b] Determined by GPC.

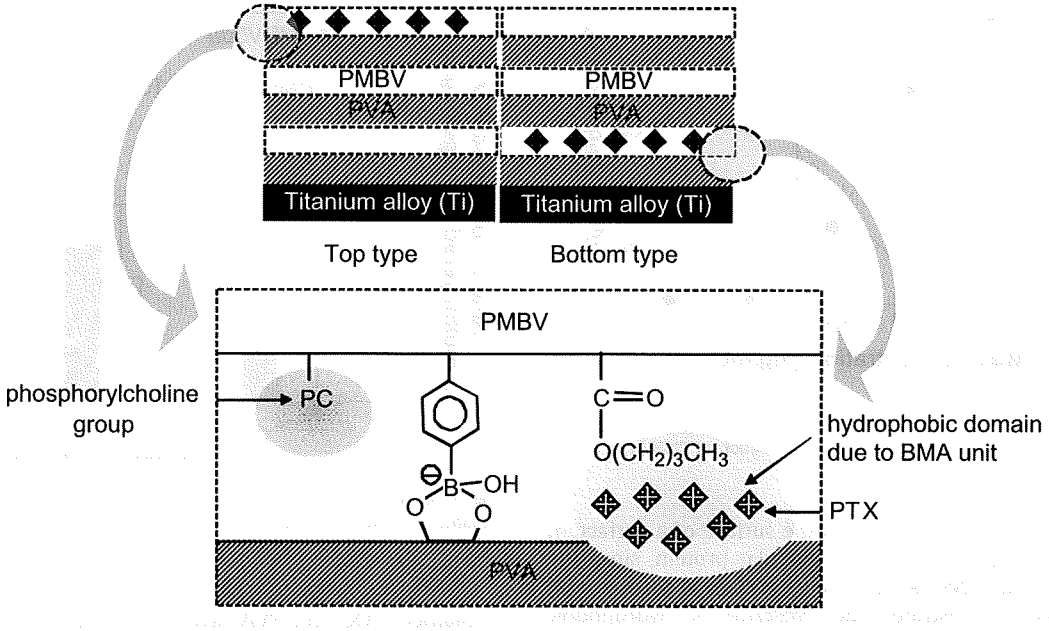

Fig. 1. Schematic representation of (a) the multilayer produced using layer-by-layer method on the Ti surface and (b) incorporated paclitaxel in bottom and top layers.

was dissolved in ethanol. The concentration of PTX in the ethanol solution was then determined by HPLC, as described previously.

2.6. Dissociation of multilayered hydrogel

Fluorescence-labeled PMBV with a small amount of pyrene, PMBVP (Fig. 2), and PVA were used to form the multilayered hydrogel in this dissociation test. Samples were submerged in 1 mL of phosphate-buffered saline (PBS, pH 7.1) containing 0.1% Tween 20. The concentration of PMBVP released was measured by fluorescence spectroscopy (ND-3300, NanoDrop Technologies, Inc., USA). At set time intervals, the PBS solution was replaced with fresh PBS. To study the morphology of the multilayered hydrogel, the samples were rinsed twice with distilled water and lyophilized. The surface morphology of the multilayered hydrogel was observed under a scanning electron microscope (SM-200; Topcon, Tokyo, Japan).

2.7. In vitro PTX release measurements

Multilayered hydrogels were functionalized with PTX using two different loading schemes (Fig. 1). The loading schemes are referred to as the top and bottom types, depending on the location of the PTX layer. During the build-up of the multilayered hydrogel, PTX was introduced into the appropriate layer by dipping the Ti substrate into a PTX-containing PMBV solution. The PTX release profiles were measured as follows. The samples were submerged in 1.0 mL of PBS containing 0.1% Tween 20. At set times, the buffer was removed and 1.0 mL of fresh medium was added. The release of the PTX was monitored by HPLC.

3. Results and discussion

3.1. Solubility of PTX in PMBV aqueous solution

To determine the polarity inside the PMBV aggregates, we measured the fluorescence spectra of ANS in PMBV aqueous solutions of various concentrations. The results are shown in Fig. 3. When the concentration of PMBV increased, the fluorescence intensity of ANS strengthened and the peak wavelength reduced. The peak shift is due to hydrophobic domain formation in PMBV aggregates. ANS molecules can bind only to hydrophobic regions

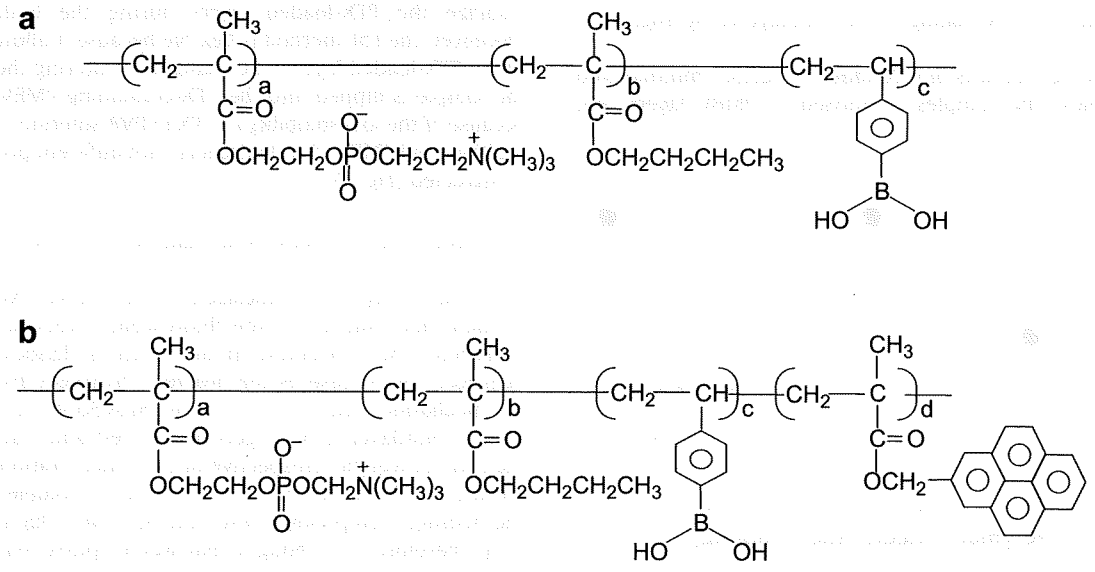

Fig. 2. Structures of (a) PMBV and (b) PMBVP.

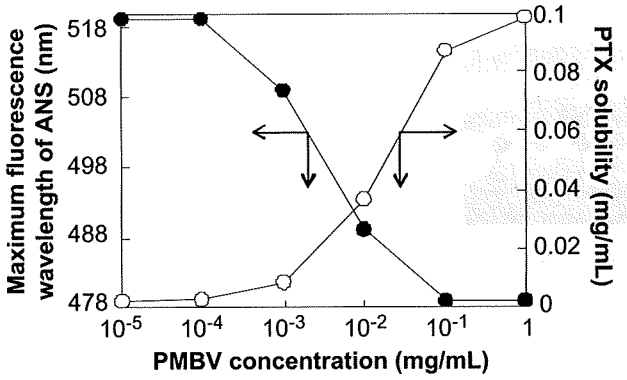

Fig. 3. Relationships between the maximum fluorescence wavelength of ANS (closed circle) and PTX solubility (open circle) and the concentration of PMBV in aqueous solution.

close to the aqueous medium, such as the surface of a surfactant micelle or the hydrophobic cleft of a globular protein, since the sulfonate group of the ANS molecule must remain in contact with water [41]. This demonstrates the presence of hydrophobic domains in PMBV aqueous solution. In addition, we found that the stronger the hydrophobicity of PMBV, the higher the solubility of PTX in PMBV aqueous solution (Fig. 3). This means that the capacity of the hydrophobic domain increases the solubility of hydrophobic agents. It has been reported that amphiphilic water-soluble MPC polymers such as PMB30W can solubilize PTX in aqueous solution without requiring a support agent because of the formation of hydrophobic domains by BMA units [41,42]. Therefore, PMBV can also play a role in dissolving PTX in hydrophobic agents.

Fig. 4 shows the amounts of PTX in the PMBV and PVA films. The polymer concentration used in this experiment was the same as that for constructing the multilayered hydrogels. The PTX concentrations in the films made using 25 and 50 mg/mL PMBV were both 0.87 mg/mL. However, because of the low solubility of PTX in PVA solutions, almost no PTX could be detected in the PVA film. Thus, the PMBV layer has the potential to serve as a drug reservoir. A multilayered hydrogel composed of PMBV and PVA could be functionalized with PTX using the difference in PTX solubility between PMBV and PVA.

3.2. Determination of PTX loading in the multilayered hydrogel

Fig. 5 shows the amounts of PTX added to various multilayered hydrogel samples. The samples comprised of PMBV layers that

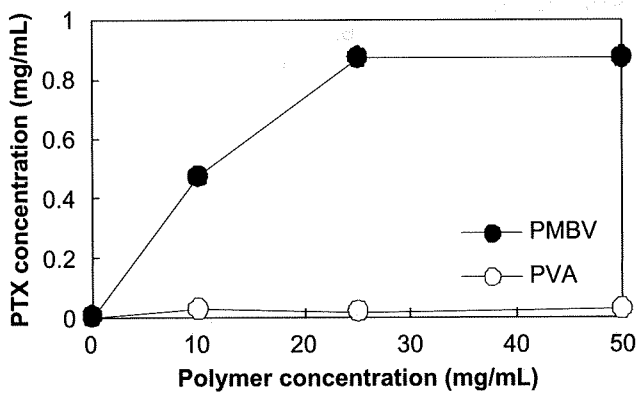

Fig. 4. Concentrations of PTX for a variety of PMBV (closed circle) and PVA (open circle) polymer concentrations. The initial concentration of PTX is 1.0 mg/mL.

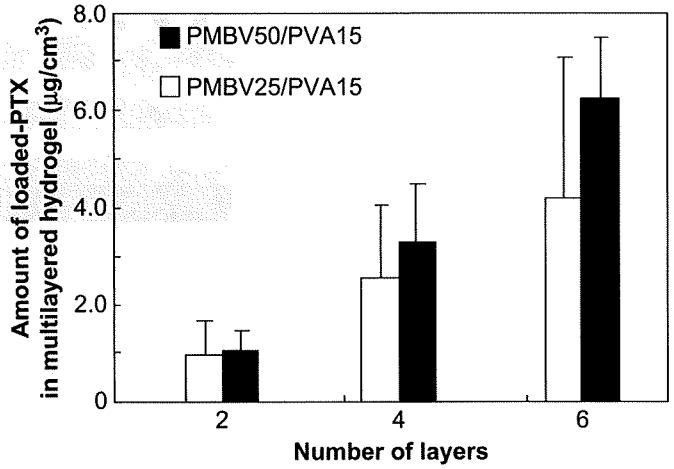

Fig. 5. Amounts of PTX loaded into multilayered hydrogel measured by HPLC. Even numbers indicate PTX loaded in a PMBV layer and odd numbers represent PVA without PTX.

contained PTX, and PVA layers that did not. By exploiting the solubility of PTX in PMBV solution, we fabricated a multilayered hydrogel network via the LbL method with simultaneous in situ drug (PTX) loading. The amount of PTX in the first PMBV layer was 1.05 μg/cm^3 for PMBV50/PVA15 and 0.98 μg/cm^3 for PMBV25/PVA15. The amount of PTX incorporated increased as a function of the number of layers. However, the total amount of PTX for three bilayers depended on the concentration of PMBV. It is thought that the concentration of PMBV is the dominant factor determining the maximum PTX loading in the PMBV layers of the multilayered hydrogels produced via the LbL method.

There are two ways of incorporating drugs into a polymeric hydrogel. One way is to incorporate the drug after the hydrogel network is formed (postloading), and the other is to simultaneously accomplish both hydrogel network formation and drug encapsulation using polymer solutions with and without the drug (in situ loading) [9]. It is difficult to incorporate a hydrophobic drug into a hydrogel matrix because of the inherent incompatibility of the hydrophilic hydrogel network and hydrophobic drug. However, amphiphilic PMBV has hydrophobic monomer units (BMA) that create hydrophobic domains within the multilayered hydrogel that stabilize the PTX-loaded layers during the build-up process. Moreover, the LbL method is flexible because it allows the location of the PTX-loaded layer to be changed by altering the timing when the sample is dipped into the PTX-containing PMBV solution, and because of the low solubility of PTX in PVA solution. In this manner, multilayered PMBV–PVA hydrogels with different properties can be constructed (Fig. 1).

3.3. Dissociation of PMBV from multilayered hydrogel

In this study, we synthesized water-soluble PMBV containing a small mole fraction of the fluorescent pyrene unit, PMBVP, to determine the concentration of polymers dissociated from the hydrogel. Fig. 6 presents the profile of hydrogel dissociation with the incubation time. Over 3 d, both PMBV50/PVA15 and PMBV25/PVA15 multilayered hydrogels dissociated and lost about 30% of their initial weight, irrespective of the concentration of PMBV. It is known that both PMBV and PVA are water-soluble polymers and the hydrogel comprising these polymers has a high swelling ratio [40]. Therefore, it is thought that water uptake leads to hydrogel dissociation. Fig. 7 shows the morphology of the multilayered hydrogels before and during incubation with PBS. Smooth surfaces

were observed initially, but pores began forming after 1 d of immersion. The pore density and size increased with the immersion period for up to 2 d.

3.4. Release of PTX from different layers of a multilayered hydrogel

The release profiles of PTX from the PMBV/PVA multilayered hydrogel are shown in Figs. 8 and 9. PTX-incorporated multilayered hydrogel on the Ti, having one of two layering schemes referred to as top and bottom types, was set in contact with PBS. To improve the solubility of PTX in the medium, 0.1% Tween 20 was added to the PBS to investigate the release behavior. All differently loaded multilayered hydrogels revealed an initial burst release within the first 7 h of immersion in PBS, ranging from 40% to 82% of the initially loaded amount of PTX (Table 2). However, the burst release was proportionally low for bottom type (40% for PMBV50/PVA15-based multilayered hydrogel) and there was a lag time for the start of PTX release particularly in the case of the bottom-type layering scheme (3 h for PMBV50/PVA15-based and 5 h for PMBV50/PVA15-based multilayered hydrogel). After the burst release, all differently loaded multilayered hydrogels had a constant rate of release, with approximately 16–38% of the remaining PTX being released over 5 d. The PTX release is summarized in Table 2. The PTX release had a two-phase pattern; that is, an initial drug burst over 7 h and a subsequent slower release phase. (a) Bulk release of 55–86% within 7 h, (b) a constant release of approximately 16–38% of the remaining PTX over the next 72 h, and (c) a lag time of 3 h or 5 h for the bottom-type layering scheme.

A simple semiempirical equation has been introduced to express general drug release behavior depending on the geometry of a system [48].

$$M_t/M_\infty = kt^n,$$

where M_t and M_∞ are the absolute cumulative amounts of drug released at time t and after the finish of release respectively, k is a diffusional kinetic constant for the characteristics of a polymer network system, and n is a diffusional exponent representing the release mechanism.

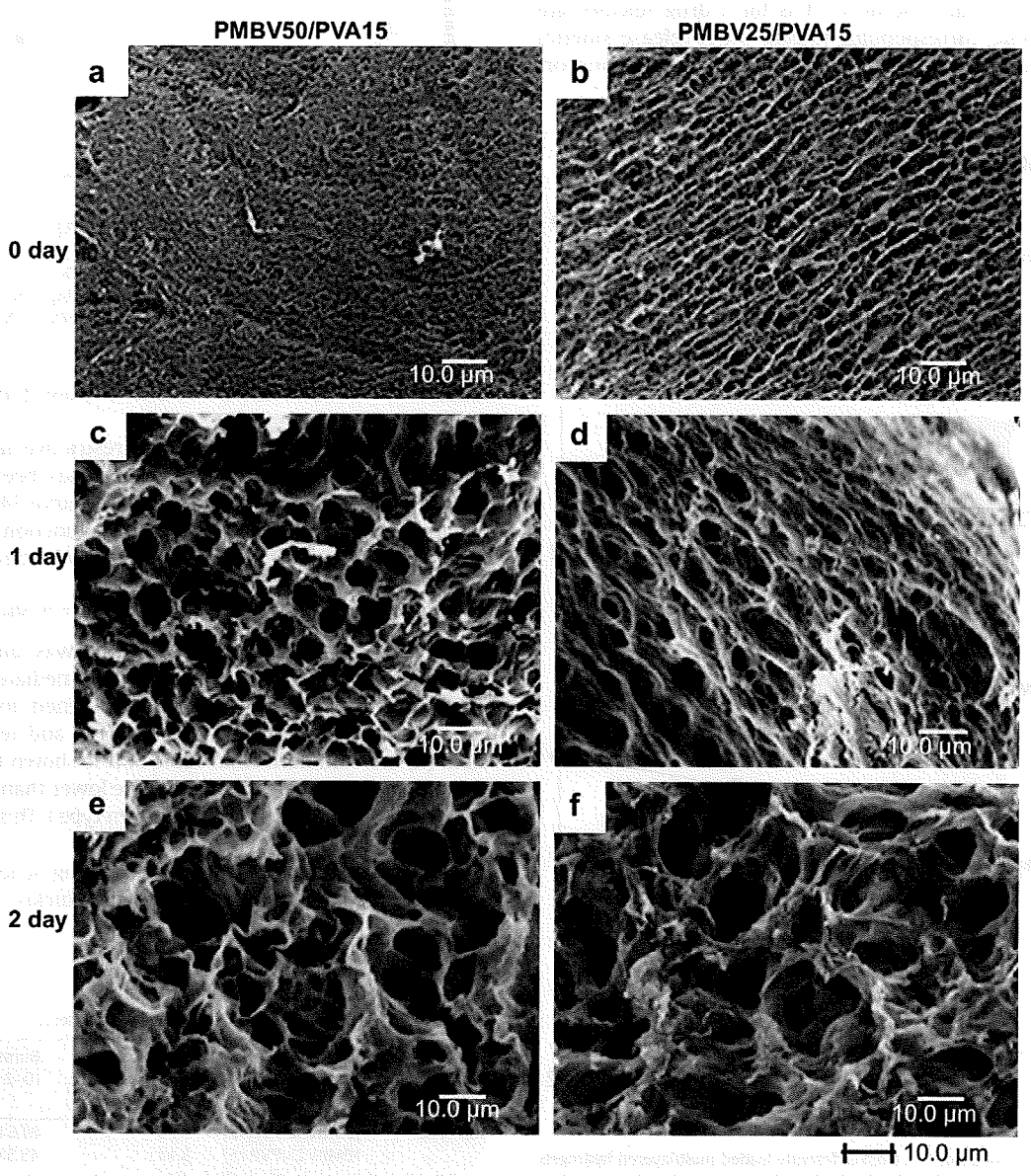

Fig. 6. SEM images of PMBV50/PVA15 and PMBV25/PVA15 multilayered hydrogels; the multilayered hydrogel dissociation in PBS (pH 7.1, 0.1% Tween 20) after (a, b) 0, (c, d) 1, and (e, f) 2 d.

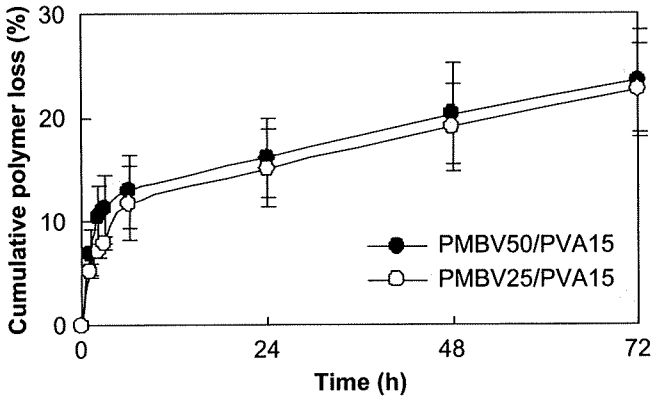

Fig. 7. Polymer dissociation in PBS (pH 7.1, 0.1% Tween 20) fluorescence-labeled PMBV (PMBVP) used for construction of the multilayered hydrogel. Polymer dissociation was estimated by fluorescence spectrometry ($n = 3$). PMBV50/PVA15 and PMBV25/PVA15 are represented by black circles (●) and white circles (○) respectively.

The case of $n = 0.5$ is for purely diffusion-controlled drug release (Fickian release) and the case of $n = 1$ is for a drug release rate independent of time, corresponding to zero-order release kinetics (Case II transport). Other values for n are for anomalous transport

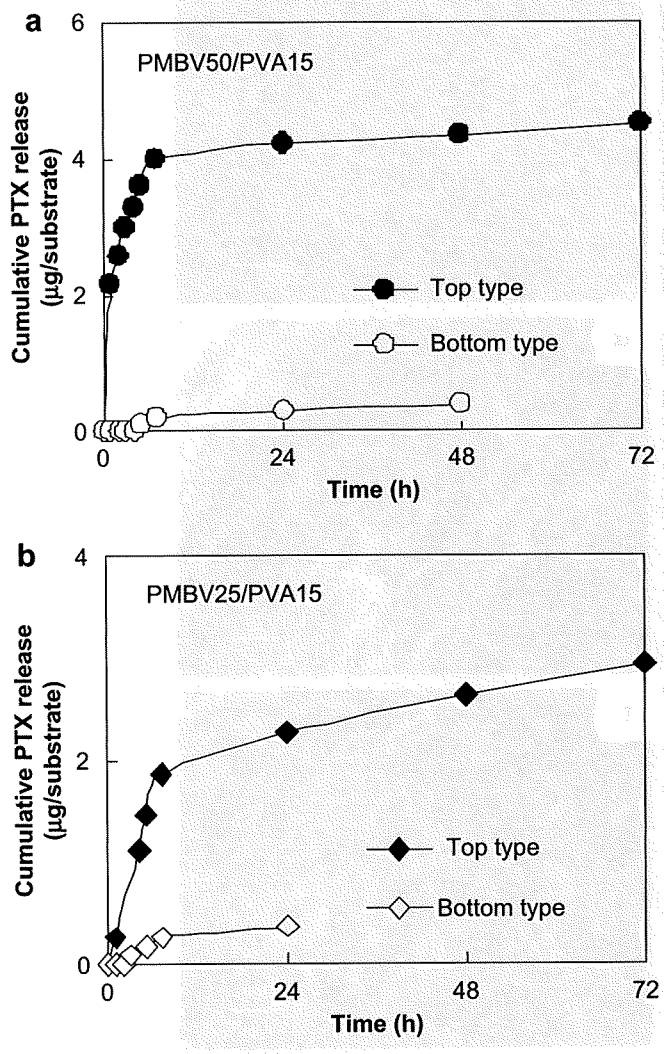

Fig. 8. In vitro release profiles of PTX from differently loaded multilayered hydrogels. Release characteristics of (a) $(PMBV50/PVA15)_6$-based multilayered hydrogel and (b) $(PMBV25/PVA15)_6$-based multilayered hydrogel. The release was conducted in phosphate buffer (pH 7.1) containing 0.1% Tween 20.

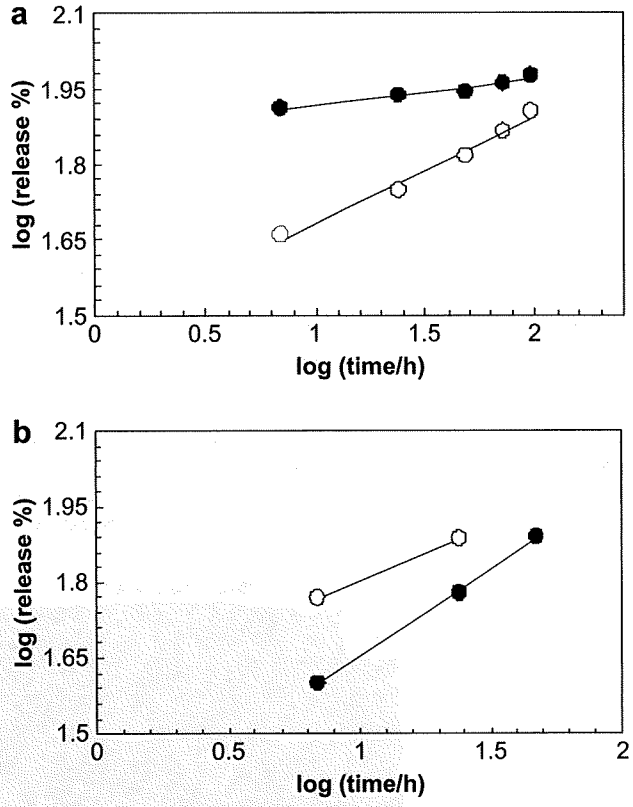

Fig. 9. In vitro release profiles of differently loaded PTX obtained from the power law model for the (a) top-type and (b) bottom-type layering schemes. The closed circles and open circles represent $(PMBV50/PVA15)_6$ and $(PMBV25/PVA15)_6$ respectively.

kinetics and combined mechanisms of pure diffusion and Case II transport.

The power law has been used for restrictive analysis of the first 60% of the release curves. However, it has been found that the power law explains the entire release curve [49,50]. The above equation can be modified as a logarithm function to obtain a linear fit for the drug release data according to Wang et al. [50].

$$\log(\text{released}\%) = \log(M_t/M_\infty) = \log k + n \log t$$

Using this equation, a good linear fit was obtained from the experimental data for PTX release from immediately after the initial burst to 100% release. The values obtained for the diffusional exponent (n), correlation coefficient (r^2), and release rate coefficient (k) are summarized in Table 3. It is shown that values of the exponent n for the release of PTX were lower than 0.5 (0.052, 0.342, 0.214, and 0.218 for top type to bottom type). This indicates Fickian release behavior.

In the case of the bottom-type layering scheme, the lag time might be explained by the different thicknesses of 8 μm for

Table 2
Release of PTX from multilayered hydrogels with different amounts of PTX loading.

PTX-loading type	Coating materials	Total amount of PTX released (μg)	Burst release (0–7 h)	Sustained release (after 7 h)
Top type	[PMBV50/PVA15]	3.95	81.6%	16.4%
	[PMBV25/PVA15]	3.48	45.5%	24.9%
Bottom type	[PMBV50/PVA15]	0.40	40.0%	37.5%
	[PMBV25/PVA15]	0.36	58.8%	18.1%

Table 3
Drug release parameters obtained from the modified power law equation.

PTX-loading type	[PMBV50/PVA15]			[PMBV25/PVA15]		
	n	k	r^2	n	k	r^2
Top type	0.052	1.865	0.946	0.214	1.467	0.983
Bottom type	0.342	1.310	0.999	0.218	1.585	1

PMBV50/PVA15 and 5 μm for PMBV25/PVA15 [40]. In addition, the initial burst was suppressed for the bottom-type layering scheme in comparison with the top type owing to the diffusion barrier. It seems that hydrogel thickness is related to the release time (lag time) and release rate, which can be controlled by the polymer concentration. On the other hand, the bottom-type layering scheme had short release times and there was no suppression of the initial burst for PMBV25/PVA15 in particular. The bottom-type layering scheme had low amounts of PTX loaded and a thick diffusion barrier in comparison with the top type. Moreover, the dissolution rate of hydrogel was not related to the polymer concentration in constructing multilayered hydrogel.

Consequently, the concentration of PTX that diffused from within might reach equilibrium earlier than that of the top type because of entrapment in the hydrogel. It is also thought that in the case of PMBV25/PVA15, the diffusion barrier dissolved quickly compared with the case of PMBV50/PVA15. Therefore, the release of PTX from multilayered hydrogel might be governed by diffusion owing to the different drug concentrations and thicknesses of the PTX-loaded layer excluding the initial burst region, and dissociation of the polymer hydrogel. Furthermore, we have investigated whether the concentration of PTX released from multilayered hydrogel influences the cell response, and we found that cell proliferation can be modulated constantly depending on the loading type. We are about to report details of the regulation of cell proliferation by multilayered hydrogel in the controlled release of PTX.

4. Conclusions

A feasibility study was conducted for in situ loading of hydrophobic drugs and multilayer construction of PMBV/PVA hydrogels in order to apply localized drug delivery in metal-based biomedical devices. The results obtained show that the water-soluble phospholipid polymer selected in this work, PMBV, induces a hydrophobic domain in an aqueous environment and forms reversible covalent bonding with PVA, resulting in the simple and instantaneous formation of multilayered hydrogel via the LbL method. In addition, in situ loading of PTX during the build-up of multilayers permits the construction of biomaterials that can control the release of bioactive agents simply. In addition, it is concluded that formulations developed in this study may be considered promising systems for delivering a variety of drugs, such as proteins, genes and other therapeutic agents, via molecular interaction.

References

[1] Mani G, Feldman MD, Patel D, Agrawal CM. Coronary stents: a materials perspective. Biomaterials 2007;28:1689–710.
[2] Acharya G, Park K. Mechanisms of controlled drug release from drug-eluting stents. Adv Drug Deliv Rev 2006;58:387–401.
[3] Kobayashi K, Ohuchi K, Hoshi H, Morimoto N, Iwasaki Y, Takatani S. Segmented polyurethane modified by photopolymerization and cross-linking with 2-methacryloyloxyethyl phosphorylcholine polymer for blood-contacting surfaces of ventricular assist devices. J Artif Organs 2005;8:237–44.
[4] Cooper MA. Optical biosensors in drug discovery. Nat Rev 2002;1:515–28.
[5] Adhikari B, Majumdar S. Polymers in sensor applications. Prog Polym Sci 2004;29:699–766.
[6] Moro T, Takatori Y, Ishihara K, Konno T, Takigawa Y, Matushita T, et al. Surface grafting of artificial joints with a biocompatible polymer for preventing periprosthetic osteolysis. Nat Mater 2004;3:829–36.
[7] Kyomoto M, Moro T, Konno T, Takadama H, Yamawaki N, Kawaguchi H, et al. Enhanced wear resistance of modified cross-linked polyethylene by grafting with poly(2-methacryloyloxyethyl phosphorylcholine). J Biomed Mater Res 2007;82A:10–7.
[8] Langer R. Polymer-controlled drug delivery systems. Acc Chem Res 1993; 26:537–42.
[9] Lin C, Metters A. Hydrogels in controlled release formulations: network design and mathematical modeling. Adv Drug Deliv Rev 2006;58:1379–408.
[10] Zhanga R, Tanga M, Bowyerb A, Eisenthalc R, Hubblea J. A novel pH- and ionic-strength-sensitive carboxy methyl dextran hydrogel. Biomaterials 2005;26:4677–83.
[11] Kim YH, Bae YH, Kim SW. pH/temperature-sensitive polymers for macromolecular drug loading and release. J Controlled Release 1994;28:143–52.
[12] Brannon-Peppas L, Peppas N. Equilibrium swelling behavior of dilute ionic hydrogels in electrolytic solutions. J Controlled Release 1991;16:319–30.
[13] Alvarez-Lorenzo C, Concheiro A, Dubovik AS, Grinberg NV, Burova TV, Grinberg VY. Temperature-sensitive chitosan-poly (*N*-isopropylacrylamide) interpenetrated networks with enhanced loading capacity and controlled release properties. J Controlled Release 2005;102:629–41.
[14] Frimpong RA, Fraser S, Hilt JZ. Synthesis and temperature response analysis of magnetic-hydrogel nanocomposites. J Biomed Mater Res 2007;80A:1–6.
[15] Qiu Y, Park K. Environment-sensitive hydrogels for drug delivery. Adv Drug Deliv Rev 2001:321–39.
[16] Berg MC, Zhai L, Cohen RE, Rubner MF. Controlled drug release from porous polyelectrolyte multilayers. Biomacromolecules 2006;7:357–64.
[17] Decher G, Hong JD, Shimit J. Buildup of ultrathin multilayer films by a self--assembly process: III. Consecutively alternating adsorption of anionic and cationic polyelectrolytes on charged surfaces. Thin Solid Films 1992;210: 831–5.
[18] Ren K, Ji J, Shen J. Construction and enzymatic degradation of multilayered poly-L-lysine/DNA films. Biomaterials 2006;27:1152–9.
[19] Zhang J, Senger B, Vautier D, Picart C, Schaaf P, Voegel J, et al. Natural polyelectrolyte films based on layer-by-layer deposition of collagen and hyaluronic acid. Biomaterials 2005;26:3353–61.
[20] Wood K, Boedecker J, Lynn D, Hammond P. Tunable drug release from hydrolytically degradable layer-by-layer thin films. Langmuir 2005;21: 1603–9.
[21] Jewell C, Zhang J, Fredin NJ, Lynn D. Multilayered polyelectrolyte films promote the direct and localized delivery of DNA to cells. J Controlled Release 2005;106:214–23.
[22] Schneider A, Vodouhê C, Richert L, Francius G, Guen E, Schaaf P, et al. Multifunctional polyelectrolyte multilayer films: combining mechanical resistance, biodegradability, and bioactivity. Biomacromolecules 2007;8:139–45.
[23] Etienne O, Gasnier C, Taddei C, Voegel J, Aunis D, Schaaf P, et al. Antifungal coating by biofunctionalized polyelectrolyte multilayered films. Biomaterials 2005;26:6704–12.
[24] Gangloff S, Ladam G, Dupray V, Fukase K, Brandenburg K, Guenounou M, et al. Biologically active lipid A antagonist embedded in a multilayered polyelectrolyte architecture. Biomaterials 2006;27:1771–7.
[25] Vodouhê C, Schmittbuhl M, Boulmedais F, Bagnard D, Vautier D, Schaaf P, et al. Effect of functionalization of multilayered polyelectrolyte films on motoneuron growth. Biomaterials 2005;26:545–54.
[26] van den Beucken JJJP, Walboomers XF, Boerman OC, Vos MRJ, Sommerdijk NAJM, Hayakawa T, et al. Functionalization of multilayered DNA-coatings with bone morphogenetic protein 2. J Controlled Release 2006;113:63–72.
[27] Rowinsky E, Donehower R. Paclitaxel (Taxol). N Engl J Med 1995;13:1004–14.
[28] Singla AK, Garg A, Aggarwal D. Paclitaxel and its formulation. Int J Pharm 2002;235:179–92.
[29] Sawada S, Iwasaki Y, Nakabayashi N, Ishihara K. Stress response of adherent cells on a polymer blend surface composed of a segmented polyurethane and MPC copolymers. J Biomed Mater Res 2006;79A:479–84.
[30] Ishihara K, Nomura H, Mihara T, Kurita K, Iwasaki Y, Nakabayashi N. Why do phospholipid polymers reduce protein adsorption? J Biomed Mater Res 1998;39:323–30.
[31] Ishihara K, Aragaki R, Ueda T, Watanabe A, Nakabayashi N. Reduced thrombogenicity of polymers having phospholipid polar groups. J Biomed Mater Res 1990;24:1069–77.
[32] Ishihara K, Ziats NP, Tierney BP, Nakabayashi N, Anderson JM. Protein adsorption from human plasma is reduced on phospholipid polymer. J Biomed Mater Res 1991;25:1397–407.
[33] Ishihara K, Oshida H, Ueda T, Endo Y, Watanabe A, Nakabayashi N. Hemocompatibility of human whole blood on polymers with phospholipid polar group and its mechanism. J Biomed Mater Res 1992;26:1543–52.
[34] Ueda T, Oshida H, Kurita K, Ishihara K, Nakabayashi N. Preparation of 2-methacryloyloxyethyl phosphorylcholine copolymers with alkyl methacrylates and their blood compatibility. Polym J 1992;24:1259–69.
[35] Chan KH, Armstrong J, Withers S, Malik N, Cumberland DC, Gunn J, et al. Vascular delivery of c-myc antisense from cationically modified phosphorylcholine coated stents. Biomaterials 2007;28:1218–24.
[36] Burke SE, Kuntz RE, Schwarts LB, Zotarolimus. (ABT-578) eluting stents. Adv Drug Deliv Rev 2006;58:437–46.

[37] Lewis AL, Vick TA, Collias AC, Hughes LG, Palmer RR, Furze SWJD, et al. Phosphorylcholine-based polymer coatings for stent drug delivery. J Mater Sci Mater Med 2001;12:865–70.
[38] Ye SH, Watanabe J, Takai M, Iwasaki Y, Ishihara K. Design of functional hollow fiber membranes modified with phospholipid polymers for application in total hemopurification system. Biomaterials 2005;26:5032–41.
[39] Konno T, Ishihara K. Temporal and spatially controllable cell encapsulation using a water-soluble phospholipid polymer with phenylboronic acid moiety. Biomaterials 2007;28:1770–7.
[40] Choi J, Konno T, Matsuno R, Takai M, Ishihara K. Surface immobilization of biocompatible phospholipid polymer multilayered hydrogel on titanium alloy. Colloid Surf B 2008;67:216–23.
[41] Ishihara K, Iwasaki Y, Nakabayashi N. Polymeric lipid nanosphere consisting of water-soluble poly(2-methacryloyloxyethyl phosphorylcholine-*co*-*n*-butyl methacrylate). Polym J 1999;31:1231–6.
[42] Konno T, Watanabe J, Ishihara K. Enhanced solubility of paclitaxel using water-soluble and biocompatible 2-methacryloyloxyethyl phosphorylcholine polymers. J Biomed Mater Res 2003;65A:210–5.
[43] Wada M, Jinno H, Ueda M, Ikeda T, Kitajima M, Konno T, et al. Efficacy of an MPC–BMA co-polymer as a nanotransporter for paclitaxel. Anticancer Res 2007;27:1431–5.
[44] Reisch A, Hemmerlé J, Voegel JC, Gonthier E, Decher G, Benkirane-Jessel N, et al. Polyelectrolyte multilayer coatings that resist protein adsorption at rest and under stretching. J Mater Chem 2008;18:4242–5.
[45] Kujawa P, Schmauch G, Viitala T, Badia A, Winnik FM. Construction of viscoelastic biocompatible films via the layer-by-layer assembly of hyaluronan and phosphorylcholine-modified chitosan. Biomacromolecules 2007;8:3169–76.
[46] Zhang Z, Cao X, Zhao X, Holt CM, Lewis AL, Lu JR. Controlled delivery of antisense oligodeoxynucleotide from multilayered biocompatible phosphorylcholine polymer films. J Controlled Release 2008;130:69–76.
[47] Ishihara K, Ueda T, Nakabayashi N. Preparation of phospholipid polymers and their properties as polymer hydrogel membranes. Polym J 1990;22:355–60.
[48] Siepmann J, Peppas NA. Modeling of drug release from delivery systems based on hydroxypropyl methylcellulose (HPMC). Adv Drug Deliv Rev 2001;48:139–57.
[49] Rinaki E, Valsami G, Macheras P. The power law can describe the 'entire' drug release curve from HPMC-based matrix tablets: a hypothesis. Int J Pharm 2003;55:199–207.
[50] Wang X, Hu X, Daley A, Rabotyagova O, Cebe P, Kaplan DL. Nanolayer biomaterial coatings of silk fibroin for controlled release. J Controlled Release 2007;121:190–9.

Biomaterials 30 (2009) 1413–1420

Contents lists available at ScienceDirect

Biomaterials

journal homepage: www.elsevier.com/locate/biomaterials

Surface modification by 2-methacryloyloxyethyl phosphorylcholine coupled to a photolabile linker for cell micropatterning

Kihoon Jang [a], Kae Sato [a,c], Kazuma Mawatari [d], Tomohiro Konno [b], Kazuhiko Ishihara [b,c], Takehiko Kitamori [a,c,d,*]

[a] Department of Applied Chemistry, School of Engineering, The University of Tokyo, 7-3-1 Hongo, Bunkyo, Tokyo 113-8656, Japan
[b] Department of Materials Engineering, School of Engineering, The University of Tokyo, 7-3-1 Hongo, Bunkyo, Tokyo 113-8656, Japan
[c] Center for NanoBio Integration, The University of Tokyo, 7-3-1 Hongo, Bunkyo, Tokyo 113-8656, Japan
[d] Kanagawa Academy of Science and Technology (KAST), KSP East307 Sakado, Takatsu-ku, Kawasaki, Kanagawa 213-0012, Japan

ARTICLE INFO

Article history:
Received 11 August 2008
Accepted 9 November 2008
Available online 10 December 2008

Keywords:
Cell micropatterning
Photochemical reaction
MPC polymer
Non-specific protein adsorption
Long-term stability

ABSTRACT

This report describes a new surface-treatment technique for cell micropatterning. Cell attachment was selectively controlled on the glass surface using a photochemical reaction. This strategy is based on combining 2-methacryloyloxyethyl phosphorylcholine (MPC) polymer, which is known to reduce non-specific adsorption, and a photolabile linker (PL) for selective cell patterning. The MPC polymer was coated directly on the glass surface using a straightforward surface modification method, and was removed by ultraviolet (UV) light illumination. All the surface modification steps were evaluated using static water contact angle measurements, X-ray photoelectron spectroscopy (XPS), atomic force microscopy (AFM), measurements of non-specific protein adsorption, and the cell attachment test. After selective cleavage of the MPC polymer through the photomask, cells attached only to the UV-illuminated region where the MPC polymer was removed, which made the hydrophilic surface relatively hydrophobic. Furthermore, the size of the MC-3T3 E1 cell patterns could be controlled by single cell level. Stability of the cell micropatterns was demonstrated by culturing MC-3T3 E1 cell patterns for 5 weeks on glass slide. The micropatterns were stable during culturing; cell viability also was verified. This method can be a powerful tool for cell patterning research.

1. Introduction

Interest in micropatterning of cells on substrate has been growing recently because of its broad range of applications, particularly for cell-based bioassay [1], tissue engineering [2], fundamental studies of cell biology [3], and cell-based drug screening [4]. To maintain the micropatterning, the spatial distribution, shape, and number of cells, and the distance between cells must remain stable for several weeks [5]. In addition, multi-step micropatterning is sometimes required to micropattern different types of cells or to increase the micropatterning area after differentiation. This novel micropatterning method shows promise from application to processes such as the analysis of chemicals released from a single cell and the communication between different cells.

Most cell micropatterning methods focus on interactions between cells and surfaces to control cell adhesiveness. Therefore, it is essential to modify materials that repel biological molecules such as proteins and cells. The conventional non-biofouling compounds include poly(2-methacryloyloxyethyl phosphorylcholine) (MPC) polymers [6–8], poly(ethylene glycol) (PEG) and its copolymer with poly(propylene oxide) (Pluronic) [9], or poly(acrylamide) [10]. MPC polymers have been used frequently to repel biological molecules. The MPC unit contains a phospholipid polar group that is also present in biomembranes, and many researchers have reported that MPC polymers inhibited not only protein adsorption but also cell adhesion. For cell attachment on surfaces, extracellular matrix (ECM) proteins such as fibronectin, collagen, laminin, matrigel, or cell-interactive peptides have been used.

Many studies of cell micropatterning have reported the control of surface properties through soft lithography [11–13], photolithography [14–16] techniques, photochemistry [17–20], and electrochemistry [21,22], which introduce or eliminate anti-biofouling compounds within a specific area. Among these techniques, photochemistry and electrochemistry can be used for multi-step micropatterning that changes cell adhesiveness and the

* Corresponding author. Department of Applied Chemistry, School of Engineering, The University of Tokyo, 7-3-1 Hongo, Bunkyo, Tokyo 113-8656, Japan. Tel.: +81 3 5841 7231; fax: +81 3 5841 6039.
E-mail address: kitamori@icl.t.u-tokyo.ac.jp (T. Kitamori).

0142-9612/$ – see front matter © 2008 Elsevier Ltd. All rights reserved.
doi:10.1016/j.biomaterials.2008.11.013

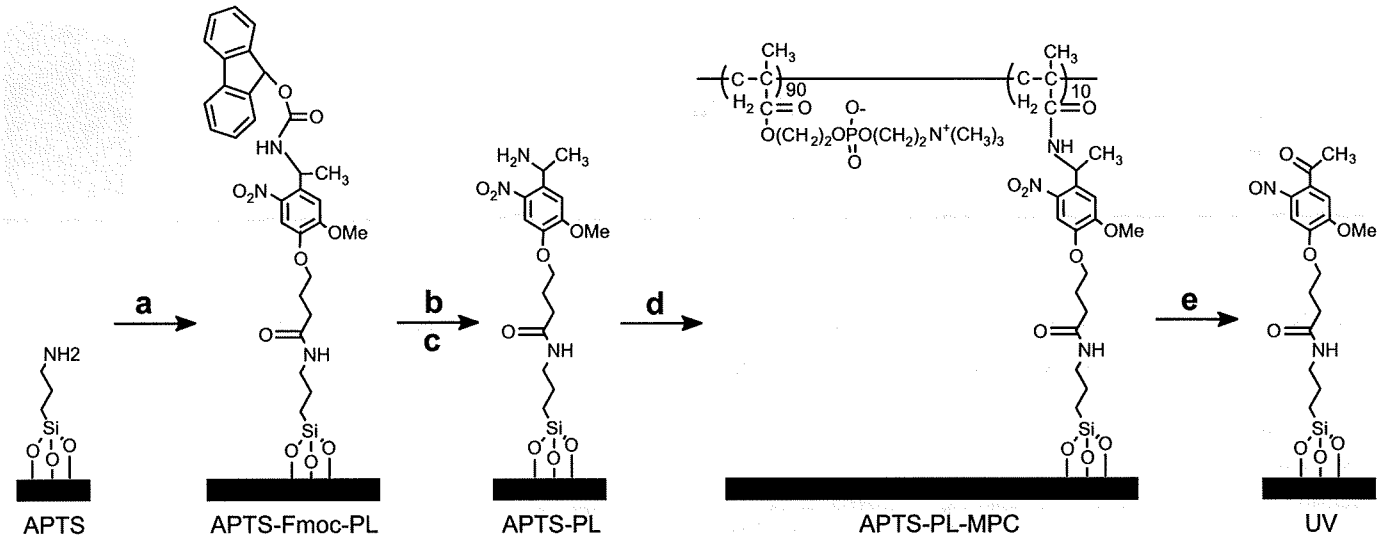

Fig. 1. Preparation of the photolabile linker-MPC polymer-modified surface: (a) Fmoc-photolabile linker (5 mM), BOP (5 mM), HOBt (5 mM), DIEA (5 mM) in DMF; (b) 30% (v/v) acetic anhydride in DCM (c) 20% (v/v) piperidine in DMF (d) MPC-*co*-MA (2.5%), EDC (0.02 M) in MOPS buffer (0.1 M, pH 5.0); (e) UV illumination (365 nm, 500 mW/cm^2).

attachment area of the cell patterns. Furthermore, external stimuli such as UV and electricity were used to localize two different types of cells on the same surface [23,24]. However, no reports have been published about the long-term stability of cell micropatterns using these strategies. These methods are thought to use physical adsorption of the anti-biofouling compound to the surface, which is too weak to withstand protein adherence for long-term culture and would result in break-up of the cell patterns. For long-term stability of pattern cells, anti-biofouling compounds should be connected with covalent bonds. A few reports on cell pattern stability for long-term culture have used photolithography with chemical bonding of the anti-biofouling materials to surfaces [25–27].

The surface modification techniques described here use chemical bonding to regulate stable cell attachment for long-term culturing on a glass surface. MPC polymer, photo-cleavable linker (PL) [23,28–32], and silanization reagents are chemically immobilized on the glass surface. UV light removes the MPC polymers from the PL, and a hydrophobic surface is formed that acts as a cell-adherent surface. Upon surface wetting, cells are effectively attached to the surface with moderate hydrophilicity [33,34]. This property was targeted to achieve selective cell micropatterning. By utilizing MPC polymers, long-term stability (several weeks) of cell adherence could be achieved. In addition, micropatterning of a cell-adherent surface is achieved by simply irradiating with UV light, permitting multi-step micropatterning to be performed.

2. Materials and methods

2.1. Chemical and biochemical reagents

3-Aminopropyltriethoxysilane (APTS), *N,N*-diisopropylethylamine (DIEA), Dulbecco's modified Eagle's medium (DMEM), fetal bovine serum (FBS), penicillin/streptomycin, phosphate-buffered saline (PBS), and fluorescein isothiocyanate-conjugated bovine serum albumin (FITC-BSA) were purchased from Sigma–Aldrich Co. (St. Louis, MO). The EC culture medium (EBM-2 supplemented with EGM-2 SingleQuots) was obtained from Cambrex (East Rutherford, NJ). HEPES, trypsin, and tripsin inhibitor were purchased from Kurabo (Osaka, Japan). Fmoc-photolabile linker [4-(4-(1-(9-fluorenylmethoxycarbonylamino)ethyl-2-methoxy-5-nitrophenoxy)-butanoic acid)] was obtained from Advanced ChemTech (Louisville, KT). Benzotriazol-1-yloxy-tris(dimethylamino)phosphonium hexafluorophosphate (BOP), 1-hydroxy-benzotriazole (HOBt), 1-[3[(dimethylamino)propyl]-3-ethylcarbodiimide hydrochloride (EDC), and piperidine were purchased from TCI (Tokyo, Japan). 3-Morpholinopropanesulfonic acid (MOPS) was purchased from Dojindo (Kumamoto, Japan). Trypsin–EDTA was purchased from Gibco (Langley, OK). Dichloromethane (DCM), *N,N*-dimethylformamide (DMF), and 0.1 M NaOH aqueous solution were obtained from Wako Pure Chemical Industries (Osaka, Japan). Poly[2-methacryloyloxyethyl phosphorylcholine (MPC)-*co*-methacrylic acid (MA)] (M_w = 100 K, MPC: 90 mol%, methacrylic acid: 10 mol%) was synthesized by the conventional radical polymerization technique.

2.2. Surface modification of cover glass slide

Preparation of the MPC polymer-modified surface is shown in Fig. 1. The cover glass slides (18 mm × 18 mm, thickness 0.12–0.17 mm, Matsunami) were precleaned in 0.1 M NaOH aqueous solution at room temperature (RT) for 20 min and then rinsed with de-ionized water and dried under a nitrogen flow. The surface was

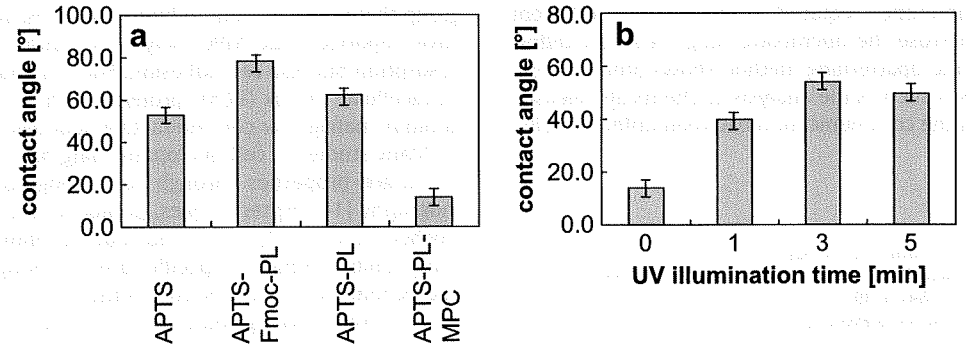

Fig. 2. (a) Static water contact angles on modified glass surface. (b) Effect of UV illumination time on the contact angles of a glass surface modified with MPC polymer. The error bars represent standard deviations.

Table 1
XPS surface composition of the modified glass surface.

Surface condition	Surface atomic composition (at%)			
	C (1s)	O (1s)	N (1s)	P (2p)
Cleaned glass	16.00	83.40	n.d.	n.d.
APTS	25.84	70.99	3.17	n.d.
APTS-Fmoc-PL	41.18	52.58	6.24	n.d.
APTS-PL	20.34	77.56	2.11	n.d.
APTS-PL-MPC	38.74	54.11	5.20	1.95
UV (3 min)	32.73	64.78	2.48	n.d.

n.d.: not detected.

aminated with 5% (v/v) APTS in chloroform at RT for 2 h, washed with chloroform, ethanol, and then de-ionized water vigorously and dried under a nitrogen flow. The aminated surface was then coupled with 5 mM Fmoc-photolabile linker, 10 mM BOP, HOBt, and DIEA in DMF at RT for 3 h to prepare a photoactive surface, and washed with DMF and de-ionized water, and dried under a nitrogen flow. After coupling of the Fmoc-photolabile linker, 30% (v/v) acetic anhydride in DCM was used at RT for 30 min to inactivate all unreacted amino groups, washed with DCM, ethanol, and de-ionized water, and dried under a nitrogen flow. The Fmoc protecting groups were then removed using 20% (v/v) piperidine in DMF at RT for 30 min, followed by washing with DMF and de-ionized water, and drying under a nitrogen flow. Surface modification using the MPC polymer containing methacrylic acid was conducted in 2.5% MPC-*co*-MA, 0.02 M EDC in 0.1 M MOPS buffer (pH 5.0) at RT for 12 h, and washed with de-ionized water, following by drying under a nitrogen flow. The MPC polymer-modified surface was exposed to UV light (365 nm, 500 mW/cm^2) with or without a photomask (chrome patterns on quartz), which was manufactured by Toppan Printing Co. Ltd. (Tokyo, Japan).

2.3. Measurement of contact angle

The surface-modified glass slide was placed on the stage of a contact angle meter (DropMaster500, Kyowa Interface Science, Saitama, Japan) and a drop of water was set on the sample surface. The static contact angle of the drop on the surface was measured at RT. At least eight contact angles from different areas were measured and averaged.

To determine the optimal UV illumination time, the contact angle of the surface versus UV illumination time was determined. UV irradiation was produced with Spot UV Curing Equipment (USHIO, Yokohama, Japan) from a distance of 4 cm (365 nm, 500 mW/cm^2). The cover glass surface then was washed vigorously with de-ionized water, and dried under a nitrogen flow. Measurements were done as described above.

2.4. Measurement of surface atomic composition by X-ray photoelectron spectroscopy (XPS)

The surface-modified glass samples were inserted in the holder of an XPS instrument (AXIS-His, Shimadzu/Kratos, Kyoto, Japan). After evacuation, measurements were obtained at 3×10^{-9} Torr. The X-ray source was Cu Kα, applied voltage was 12 kV, and electric current was 10 mA. The take-off angle of the photoelectrons was 90°.

2.5. Measurement by atomic force microscopy (AFM)

The topography of the modified glass surfaces was observed with an atomic force microscope (SPA-400, SII NanoTechnology, Tokyo, Japan). Surface topography was evaluated for areas of 10 μm × 10 μm using Nanoscope program. Surface roughness was estimated by the root mean square (RMS) average of height deviation taken from the mean data plane. The average of the three measurements ($n = 3$) was recorded.

2.6. Measurement of non-specific protein adsorption

Quantitative measurements were performed on round cover glass slides (diameter: 12 mm, thickness: 0.15 mm) with BSA and fibronectin using the following procedure. The surface-modified glass slides were dipped in 10 mL of protein solution (0.32 mg/mL) – the protein concentration of both the BSA and fibronectin solutions was the same – followed by incubation at 37 °C for 1 h. Then, the glass slides were washed twice with de-ionized water for 3 min each while stirring at 300 rpm. To detach all the adsorbed proteins from the glass, each slide was placed in a small vial bottle with 2 mL BSA solution and 0.5 mL fibronectin solution in 1 wt% sodium dodecyl sulfate (SDS) (water as solvent), followed by ultrasonication for 10 min. The amount of protein in the SDS solution was calculated using the BCA (bicinchoninic acid) protein assay (micro BCA protein assay reagent kit: Pierce Biotechnology) protocol.

2.7. Preparation of MC-3T3 E1 cells

MC-3T3 E1 cells were cultured in 60-mm cell-culture dishes at 37 °C under 5% CO_2 using DMEM supplemented with 10% FBS, 1% penicillin, and 1% streptomycin. After MC-3T3 E1 cells became confluent, they were washed with 2 mL of PBS and immersed for 2 min in 1 mL of trypsin to detach them. The detached cells were added to fresh DMEM and the cell suspension was centrifuged at 1100 rpm for 5 min. Finally, the supernatant was aspirated and MC-3T3 E1 cells were re-suspended in DMEM for the following experiments.

2.8. Measurements of cell attachment on modified surfaces

All surface modification steps were introduced on glass slide (4 mm × 4 mm, thickness 1 mm, Matsunami). The prepared cover glass surface was placed into a 30-mm cell-culture dish, sterilized with ethanol, and then washed with de-ionized water. The water then was removed by suction. A cell suspension (1×10^4 cells/mL, 20 μL) was seeded on the surface-modified glass surface and incubated under 5% CO_2 at 37 °C. After 2 h of incubation, unattached cells were washed off with medium and the cells observed under a microscope. To calculate the number of attached cells on the modified surface, measurements were taken at the center (2 mm × 2 mm) of the slide glass. Cell counts were converted to cell density per area (cells/mm^2).

2.9. Protein micropatterning

After confirming the optimal UV irradiation time, irradiation by UV of the modified surface was done through the photomask, followed by washing with de-ionized water. FITC-BSA (10 mg/mL) was dissolved in PBS, and sterilized by filtration (0.22 μm). The FITC-BSA solution was dropped onto the UV-illuminated surface at RT and reacted for 50 min. After washing vigorously with PBS and de-ionized water, and drying, the sample surface was observed under a fluorescence microscope.

2.10. Cell micropatterning

The preparation of the UV-illuminated surfaces was accomplished as described above. Cell micropatterning was performed with MC-3T3 E1 cells. Photomasks in the shape of a stripe (200 μm) and round (30 μm and 50 μm) were used. The prepared cover glass was placed into a 30-mm cell-culture dish and sterilized with 70% (v/v) ethanol for 30 min, then washed with de-ionized water. The water was removed by suction, and 100 μL cell suspension (stripe shaped pattern: 4×10^5 cells/mL, round shaped pattern: 1×10^5 cells/mL, 100 μL) was seeded on the prepared cover glass surface and incubated under 5% CO_2 at 37 °C. After 2 h of incubation, the unattached cells were washed out with medium and cultured in an incubator under 5% CO_2 at 37 °C. The patterned cells were observed under a microscope.

2.11. Cell staining

Cell staining was performed on the 50-μm and 30-μm round shaped cell patterns. First, samples were fixed with 4% paraformaldehyde in PBS for 20 min at

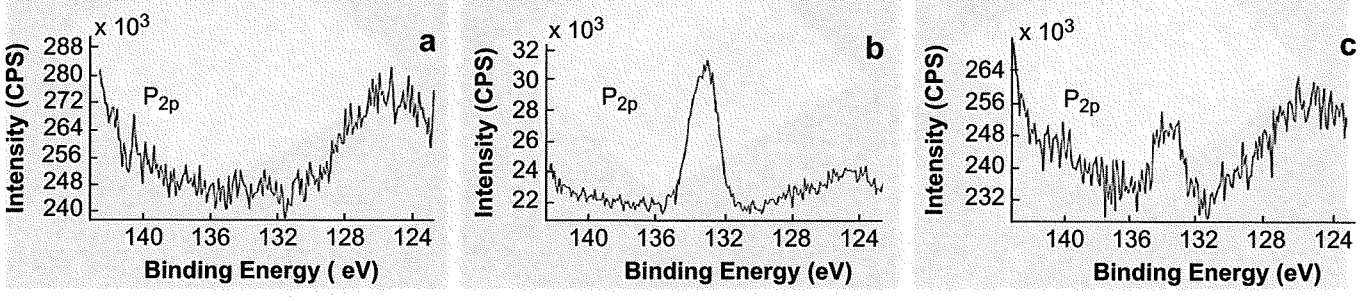

Fig. 3. XPS spectra of phosphorus element on modified glass surface (a) APTS-PL, (b) APTS-PL-MPC, (c) UV-irradiated surface.